

Numerical Simulation of Transonic Propeller Flow Using a Three-Dimensional Small Disturbance Code Employing Novel Helical Coordinates

(NASA-TM-89826) NUMERICAL SIMULATION OF
TRANSONIC PROPELLER FLOW USING A
3-DIMENSIONAL SMALL DISTURBANCE CODE
EMPLOYING NOVEL HELICAL COORDINATES (NASA)
23 p

N87-19350

Unclas
43506

CSCL 01A G3/02

Aaron Snyder
Lewis Research Center
Cleveland, Ohio

Prepared for the
8th Computational Fluid Dynamics Conference
sponsored by the American Institute of Aeronautics and Astronautics
Honolulu, Hawaii, June 9-11, 1987



NUMERICAL SIMULATION OF TRANSONIC PROPELLER FLOW USING A THREE-DIMENSIONAL SMALL DISTURBANCE CODE
EMPLOYING NOVEL HELICAL COORDINATES

Aaron Snyder*
National Aeronautics and Space Administration
Lewis Research Center
Cleveland, Ohio 44135

Abstract

This paper discusses the numerical simulation of three-dimensional transonic flow about propeller blades. The equation for unsteady potential flow about propellers is given for an arbitrary coordinate system. The small disturbance form of the equation is then derived for a new helical coordinate system. The new coordinate system is suited to propeller flow and allows cascade boundary conditions to be straightforwardly applied. A numerical scheme is employed which solves the steady flow as an asymptotic limit of unsteady flow. Solutions are presented for subsonic and transonic flow about a 5 percent thick bicircular arc blade of an eight bladed cascade. Both high and low advance ratio cases are given, and include a lifting case as well as nonlifting cases. The nonlifting cases are compared to solutions from a Euler code.

Nomenclature

A function relating periodic helical coordinates to Cartesian coordinates

A_1, A_2, \dots, A_8 coefficients of small disturbance equation, Eq. (51)

\bar{a} undisturbed fluid velocity vector in general rotating coordinate system

a_0 nonnegative constant, Eq. (38)

B function relating r to z , Eq. (32)

c_∞ speed of sound at infinity

D_γ special difference operator in mean flow direction

E damping function in helical coordinate system

F function defining blade surface

F_0, F_u lower and upper blade functions

g determinant of the metric tensor

g_{ij}, g^{ij} covariant and contravariant components of the metric tensor

h blade profile parameter

h_0, h_u lower and upper blade profiles

k ratio of specific heats

l blade chord

M radially dependent Mach number of free-stream

M_R Mach number of propeller tip at $r = R$

M_T circumferential Mach number of propeller tip at $r = R$

N number of ADI iterations

N_B number of blades in cascade

q' perturbation velocity

R radius of propeller

r radius from axis of rotation; second helical coordinate

r radius from origin

t time

t_{max} maximum thickness of blade

U helical velocity

u', v', w' perturbation fluid velocities in x, y, z -directions

\bar{V} advance velocity of propeller; relative velocity between inertial and rotating frames

X, Y, Z Cartesian coordinates in inertial frame

x, y, z Cartesian coordinates in rotating frame

x^1, x^2, x^3 Cartesian coordinates corresponding to x, y, z

y^1, y^2, y^3 helical coordinates corresponding to r, r, ϵ

Greek:

α angle of attack

Γ circulation function

γ, r, ϵ helical coordinates

$\bar{\gamma}, \bar{r}, \bar{\epsilon}$ uniform computational coordinates

Δ increment operator

δ ratio of maximum blade thickness to chord length, $\delta = t_{max}/l$

*Member AIAA.

$\delta_\gamma, \delta_{\gamma\gamma}, \dots, \delta_{\gamma\xi}$	finite difference operators
ϵ	inverse of blade aspect ratio, $\epsilon = b/R$
ϵ_j	streamwise switching operator
ϵ_{ijk}	permutation symbol
θ	circumferential angle about axis
λ	advance ratio, $\lambda = V/(\Omega R)$
ξ_m	half the distance between neighboring blades
$\bar{\xi}$	ξ as measured from nearest blade
ϕ	total velocity potential
φ	perturbation velocity potential
Ω	rotational speed of propeller
ω	frequency of airfoil motion

Subscripts and superscripts:

I, J, K	nodal indices of computational mesh
i, j, k	indices for tensor quantities
L.E.	leading edge
n, n+1	value at time step n and n+1
T.E.	trailing edge
*	value at first intermediate time step
**	value at second intermediate time step
'	derivative of quantity

Introduction

Computational fluid dynamics (CFD) has become a powerful tool in the analysis of complex fluid flows. Coinciding with the arrival of increasingly powerful CFD methods, renewed interest has emerged in propellers which offer large performance improvements for aircraft that cruise in the high subsonic speed range. This paper presents results of the numerical simulation of the flow about propeller blades operating with tip speeds in the transonic regime. These results were obtained using an ADI finite difference procedure to solve the low frequency form of the three-dimensional small disturbance equation. Expressing the small disturbance equation in terms of novel helical coordinates significantly facilitates the numerical solution for propeller flow.

Recent propeller research programs have introduced turboprops which differ considerably from their low-speed turboprop counterparts. The most notable changes are the use of eight to ten thin, highly swept, small-diameter blades instead

of two to four longer, thicker and unswept conventional blades. These changes allow propellers to operate efficiently in the transonic flow regime. However, they require sophisticated computational methods in order to predict and calculate their aerodynamic characteristics. This is mainly due to the increased three dimensionality of the flow field encompassing these low aspect ratio blades and to the rise of mathematical nonlinearity in the flow model which is associated with their transonic tip speeds. Also, their thin structural design makes them prone to flutter. This is a source of unsteadiness which must be considered in addition to the inherent unsteadiness of the transonic regime.

Many examples of both steady and unsteady flows of practical interest are well approximated by various forms of the governing equations of fluid mechanics. The recent marked advance in computer capabilities and the rapid growth of efficient and accurate numerical methods have allowed a number of previously untenable problems to be examined. The use of numerical methods offers the ability to handle complex equations with intricate geometries such as exist in the case of simulating flow about rotating propeller blades. However, as with any method, limits exist on the capabilities. These limits involve the speed and memory size of the computers and the availability of efficient algorithms as well as considerations of robustness and affordability. For a given problem, judgement dictates the trade-off between the suitability of a particular model and the feasibility of the calculation. A number of numerical codes are currently being developed to calculate propeller flow. These solve either the full potential or Euler equations. Although these equations accurately model the flow, they are computationally more expensive and more complicated to numerically code than the small disturbance equation.

A numerical code was developed¹⁻⁴ to simulate the flow over blade-tips of helicopter rotors. This code solves the small disturbance equation⁵ appropriate to a helicopter in forward flight. In particular, results were obtained that showed the code was able to track the development of a shock and its subsequent propagation upstream. The successful application of the small disturbance code in this manner indicated that the same approach could be applied to the propeller problem.

The fact that turboprops operate at high subsonic cruise speeds means that at least the tip region of each blade will be embedded in a transonic helical flow. Shocks may likely exist ahead of or on the blades, depending on the flight speed and propeller design. Shocks of high strength indicate large shock wave drag. Efficient flight dictates that only weak shocks are acceptable, which implies little entropy generation. The potential formulation should provide a good approximation to the Euler equations as long as the shock strengths are less than that of a normal shock with an upstream Mach number less than about 1.3. Presently, turboprops that have helical Mach numbers slightly less than one at the hub to about 1.12 at the tip are being designed. It is reasonable to expect that the shock strength is sufficiently weak near the blade tips, where three-dimensional relief effects occur, so that the potential formulation is adequate. Furthermore,

the use of a perturbation potential in place of a full potential significantly simplifies the formulation of the problem.

Although many similarities exist between the equations developed for the helicopter rotor and the propeller problem, fundamental differences exist between the two. These differences demand special consideration be made in accurately treating each type of flow. For example, in the case of the helicopter rotor, the flow field as observed in a coordinate system attached to the blade remains unsteady even if blade flutter is ignored. However, when the axis of rotation for a propeller coincides with its flight direction, a steady flow results with a blade-attached coordinate system. This allows the steady problem to be examined separately from the flutter or gust problem. With the goal of using the numerical algorithm developed for the rotor code to the propeller problem, several concerns need to be addressed. Many of these concerns are naturally handled by using a suitable coordinate system.

The key to simplifying the potential formulation of the propeller problem is the use of the helical free-stream direction as the primary direction. This provides an accurate primary flow upon which a perturbation can be superposed. The use of a helical flow, which inherently captures the flow curvature, results in a marked improvement over using an axial flow as the primary flow. The optimum flow to base a perturbation about is the exact flow; helical flow much more closely approximates the exact flow about a rotating and advancing propeller than does axial flow.

Since the helical flow direction captures the fundamental properties of propeller flow, relatively few terms are needed in the resulting disturbance equation to provide accurate modeling of the flow. In fact, no more terms are needed than when using Cartesian coordinates for the rotor problem. In addition, due to the similar nature of the two problems, the terms in the two sets of disturbance equations correspond identically except for their coefficients. Thus, the propeller equation is amenable to the same potential solver as developed for the helicopter code. This is quite advantageous since much effort has been expended, both in making the potential solver efficient and in verifying its operation.

While the helical flow direction is an ideal choice for the primary flow direction, other considerations must be taken into account in order to provide a satisfactory coordinate system. These considerations hinge on the desire to include cascade effects and the employment of small disturbance boundary conditions near the blade surfaces. Proper specification of the helical coordinates permits the straightforward treatment of annular cascade flows while maintaining orthogonal properties near the blade locations. The helical coordinates given in this paper allow both of these requirements to be met.

These helical coordinates are analytically defined in terms of basic propeller parameters through simple transformations to Cartesian coordinates. Thus, they automatically adapt to the cascade configuration for any number of blades and blade twist, which itself is a function of

the propeller advance ratio. The helical coordinates enter the problem in terms of the metric tensor. The components of the metric tensor are readily evaluated in a separate subroutine. The Jacobian of the transformation is particularly simple and provides a means to determine if a given transformation is valid.

Obtaining accurate solutions for steady, yet alone unsteady, three-dimensional transonic flows presents a difficult challenge even for the most advanced computational methods. The present work assumes a steady state flow exists as observed in a reference frame attached to the propeller system which is rotating with a constant angular velocity. This is considered a necessary step to be completed before undertaking the unsteady problem. In addition, the fluid will be regarded as being inviscid in an irrotational flow field which is expressible in terms of a potential formulation. The solution is sought in terms of a disturbance potential. This disturbance potential is the potential associated with the reduced velocity obtained by subtracting both the free-stream velocity and the rotational velocity, resulting from the transformation to a noninertial reference frame, from the total velocity. This solution should be valid for lightly loaded blades.

This paper presents the governing equation for the three-dimensional small perturbation potential and its derivation from the potential equation valid for a rotating reference frame. This is given in general tensor form applicable to any suitable coordinate system, which need not be orthogonal. An original helical coordinate system is then specified which aligns with the mean undisturbed flow and provides for easy application of periodic boundary conditions as well as providing appropriate surfaces on which to enforce the small disturbance boundary conditions. The small disturbance form of the equation is then presented in terms of these coordinates which are scaled by the relevant transonic scaling parameters. A generalized form of the Douglas-Gunn algorithm is given which allows for additional cross-derivative terms to be included in the potential solver. However, for the flow cases presented here, these terms had little effect on the solution, and, hence, for the results of this effort they were omitted from the governing equation.

Solutions are presented for an annular cascade consisting of eight bicircular arc blades with a maximum thickness of 5 percent. These blades are run for two geometric operating conditions: a high advance ratio case where the advancing speed is large compared to the rotational speed of the propeller tip, and a low advance ratio case where these two speeds are equal. For the high advance ratio case, the helical free-stream Mach number relative to the blade tip is $M_R = 0.8$. For the low advance ratio case, results for two values of the free-stream Mach number are presented - a subsonic free-stream case of $M_R = 0.8$, and a transonic case of $M_R = 1.1$ which is representative of a turboprop. In general, the results are for zero angle of attack; however, a lifting case is presented for the low advance ratio and high free-stream condition. The nonlifting cases are compared with results from an

Euler code. In the discussion and results sections, the abbreviation HSD will be used to denote the helical small disturbance computations.

Governing Equation

This section presents the potential equation and the development of an approximation to it which is valid for small disturbance flow about thin propeller blades which are lightly loaded. First, the potential equation in rotating coordinates will be given as developed for a coordinate system attached to a helicopter blade. Following this, the equivalent tensor equation valid for any curvilinear coordinate system will be presented for an accelerated system. Finally, the small perturbation equation for generalized helical coordinates will be given.

Potential Equation in Noninertial System

The potential equation can be expressed in vector form⁶ as

$$\phi_{tt} + \frac{\partial}{\partial t}(\nabla\phi)^2 + \frac{1}{2} \nabla\phi \cdot \nabla(\nabla\phi)^2 = c_\infty^2 - (\kappa - 1) \left[\phi_t + \frac{1}{2}(\nabla\phi)^2 \right] \quad (1)$$

where ϕ is the velocity potential, c_∞ is the upstream speed of sound and κ is the ratio of specific heats.

The potential equation can be expressed in an xyz coordinate system which is both translating with an arbitrary constant velocity \bar{V} away from the inertial frame, and rotating with an arbitrary constant rotational velocity $\bar{\Omega} \times \bar{r}$. The angular velocity vector $\bar{\Omega}$ (with magnitude Ω) has the direction of the axis through the origin about which xyz are rotating, and \bar{r} is the position vector in this system. The relationship between the two coordinate systems is shown in Fig. 1. Although both \bar{V} and $\bar{\Omega}$ are general vectors, they will soon be restricted to a common axial direction.

A potential equation can also be established in the noninertial frame. This is initiated by defining a perturbation potential φ which separates the contribution of the free-stream from the total potential. The free-stream contains both the uniform flow and the bulk rotational flow, and

$$\bar{q}' \equiv \nabla\varphi = \bar{q} - (\bar{V} + \bar{\Omega} \times \bar{r}) \quad (2)$$

represents the irrotational perturbation velocity. The gradient operator is invariant with respect to choice of Cartesian coordinate systems. The components of the perturbation velocity \bar{q}' are defined as

$$u' = \frac{\partial\varphi}{\partial x}, \quad v' = \frac{\partial\varphi}{\partial y}, \quad w' = \frac{\partial\varphi}{\partial z} \quad (3)$$

The transformation of the potential equation has been carried out by Isom⁵ for a coordinate system translating and rotating with constant, but otherwise arbitrary, V and Ω . The potential equation in the noninertial system is given as

$$\begin{aligned} \varphi_{tt} + \bar{a} \cdot \nabla(\nabla\varphi \cdot \bar{a}) + 2\bar{a} \cdot \nabla\varphi_t - \bar{\Omega} \times \bar{a} \cdot \nabla\varphi \\ - \frac{\partial \bar{V}}{\partial t} \cdot \nabla\varphi + 2\nabla\varphi \cdot \nabla\varphi_t + \bar{a} \cdot \nabla(\nabla\varphi)^2 \\ = \left\{ c_\infty^2 - (\kappa - 1) \left[\varphi_t + \bar{a} \cdot \nabla\varphi + \frac{1}{2}(\nabla\varphi)^2 \right] \right\} \nabla^2\varphi \end{aligned} \quad (4)$$

where \bar{a} is the negative of the vector sum of the translational velocity and the rotational velocity as seen by an observer in the rotating frame. Thus, for such an observer, \bar{a} can be simply written as

$$\bar{a} = -(\bar{V} + \bar{\Omega} \times \bar{r}) \quad (5)$$

It should be pointed out that in the transformation from the potential Eq. (1) for an inertial reference frame to Eq. (4) for a noninertial frame, the cubic term, the last term on the left-hand side of Eq. (1), was dropped. Otherwise, Eq. (4) remains an exact equation. The introduction of the perturbation potential does not, in itself, imply any approximations.

Potential Equation in Noninertial Curvilinear Coordinate System

The application of Eq. (4) to the propeller problem can be carried out by further simplification in much the same manner as was done in deriving the small disturbance equations for the helicopter problem. However, since the helical coordinate systems which will be used for the propeller problem are nonorthogonal, the potential Eq. (4) is more tractable if expressed in invariant tensor form. The tensor form of Eq. (4) is

$$\begin{aligned} \frac{\partial^2 \varphi}{\partial t^2} + a^i \frac{\partial}{\partial y^i} \left(a^j \frac{\partial \varphi}{\partial y^j} \right) + 2a^i \frac{\partial^2 \varphi}{\partial y^i \partial t} \\ - \frac{1}{2} \epsilon^{ijk} (\Omega_j a_k - \Omega_k a_j) \frac{\partial \varphi}{\partial y^i} + \frac{\partial}{\partial t} \left(g^{ij} \frac{\partial \varphi}{\partial y^i} \frac{\partial \varphi}{\partial y^j} \right) \\ + a^i \frac{\partial}{\partial y^i} \left(g^{jk} \frac{\partial \varphi}{\partial y^j} \frac{\partial \varphi}{\partial y^k} \right) = \left\{ c_\infty^2 - (\kappa - 1) \left[\frac{\partial \varphi}{\partial t} + a^i \frac{\partial \varphi}{\partial y^i} \right. \right. \\ \left. \left. + \frac{1}{2} g^{ij} \frac{\partial \varphi}{\partial y^i} \frac{\partial \varphi}{\partial y^j} \right] \right\} \left[g^{ij} \frac{\partial^2 \varphi}{\partial y^i \partial y^j} + \frac{1}{\sqrt{g}} \frac{\partial}{\partial y^i} \right. \\ \left. (\sqrt{g} g^{ij}) \frac{\partial \varphi}{\partial y^j} \right] \end{aligned} \quad (6)$$

for a translational velocity \bar{V} which is independent of time. In this equation a^i and a_j represent the contravariant and covariant components of the general velocity vector \bar{a} defined by Eq. (5). The quantities g^{ij} are the contravariant components of the metric tensor for the transformation between the curvilinear coordinates y^i and our orthogonal Cartesian coordinates. The quantity g is the determinant of the corresponding covariant components of the metric tensor g_{ij} which do not appear explicitly in the equation. The symbol ϵ^{ijk} is the permutation symbol which equals zero for repeating values of i, j, k , unity for cyclic (even) permutations of 1, 2, 3, and negative unity otherwise.

Potential Equation in Helical Coordinates

Equation (6), expressed in terms of a rotating coordinate system, can be simplified considerably by choosing one of the curvilinear coordinates to be in the direction of the vector \bar{a} . From Eq. (5), this is seen to be the direction opposite the vector sum of the translational velocity and rotational velocity which we now take to be orthogonal such that \bar{V} is aligned with the axis of rotation, as shown in Fig. 2. With this arrangement the vector \bar{a} is in the direction of the free-stream velocity vector as it appears to an observer whose frame of reference rotates with the blade. In this instance the magnitude of \bar{a} will be designated by U , such that in matrix form

$$\bar{a} = \begin{bmatrix} U \\ 0 \\ 0 \end{bmatrix} \quad (7)$$

and

$$U^2 = (\Omega r)^2 + V^2 \quad (8)$$

where r is the radial distance as measured from the axis of rotation. Equation (6) then simplifies to

$$\begin{aligned} & \frac{\partial^2 \phi}{\partial t^2} + U^2 \frac{\partial^2 \phi}{(\partial y^1)^2} + 2U \frac{\partial^2 \phi}{\partial y^1 \partial t} - \frac{1}{2} \Omega^2 y^2 \frac{\partial \phi}{\partial y^2} \\ & + \frac{\partial}{\partial t} \left(g^{ij} \frac{\partial \phi}{\partial y^i} \frac{\partial \phi}{\partial y^j} \right) + U \frac{\partial}{\partial y^1} \left(g^{jk} \frac{\partial \phi}{\partial y^j} \frac{\partial \phi}{\partial y^k} \right) \\ & = \left\{ c_\infty^2 - (\epsilon - 1) \left[\frac{\partial \phi}{\partial t} + U \frac{\partial \phi}{\partial y^1} + \frac{1}{2} g^{ij} \frac{\partial \phi}{\partial y^i} \frac{\partial \phi}{\partial y^j} \right] \right\} \\ & \times \left[g^{ij} \frac{\partial^2 \phi}{\partial y^i \partial y^j} + \frac{1}{\sqrt{g}} \frac{\partial}{\partial y^i} \left(\sqrt{g} g^{ij} \right) \frac{\partial \phi}{\partial y^j} \right] \quad (9) \end{aligned}$$

Approximate Potential Equation in Scaled Helical Coordinates

Equation (9) is exact in that it is equivalent to Eq. (4), but expressed in a blade-fixed reference system. However, this equation is much too complicated to be solved efficiently. Therefore, a systematic simplification is necessary to arrive at an approximation which retains the nonlinear features of the problem and which is valid for small disturbances about the mean flow. Starting from Eq. (4), such a procedure was carried out by Isom⁵ using Cartesian coordinates for flow about the tip region of a helicopter blade. Following the development of the approximate equation for the helicopter problem, a similar process is

applied to Eq. (6) for the case of a propeller blade using helical coordinates. The use of helical coordinates introduces the metric tensor into the approximate equation and allows representation of flow curvature.

The derivation of the approximate equations for flow about a propeller is based on consideration of the following parameters: the free-stream axial Mach number M_∞ ; the thickness ratio δ ; the ratio of the chord ℓ to the blade-tip radius R , which is the inverse of the aspect ratio, ϵ ; and the advance ratio λ . For true unsteady problems the reduced frequency would enter; however, since we are examining only steady solutions, the reduced frequency need not be introduced. Also, for cascade solutions, a parameter representing the blockage of the flow, say solidity, would normally enter; here the blades will be considered far enough apart that variations in solidity will not be important. For an advanced turboprop, typical values of the parameters are $M_\infty = 0.8$, $\delta = 0.02$, $\epsilon = 0.3$, and $\lambda = 1$.

The lateral direction y^3 , which lies essentially normal to the blade, is scaled by dividing it by the value $\delta^{1/3}$. This could be done for the radial-like or spanwise direction y^2 , also since the physical justification for scaling is to transform the lateral dimensions to account for the weak diminution of disturbances in these directions in comparison to the streamwise direction. However, Isom chose to scale the spanwise direction differently by introducing ϵ . This is accomplished by normalizing the streamwise direction y^1 along with the already scaled y^3 direction by ℓ , while normalizing y^2 by R . Since these two methods of scaling the y^i result in the same final approximation, either can be used. The latter choice is made here and the directions are scaled such that the original coordinates transform to the dimensionless ones, as given by

$$y^1 = \ell \tilde{y}^1, \quad y^2 = R \tilde{y}^2, \quad y^3 = \frac{\ell}{\delta^{1/3}} \tilde{y}^3 \quad (10)$$

where the tilde denotes the dimensionless coordinates. In addition, time and the disturbance potential are nondimensionalized as follows:

$$t = \frac{\tilde{t}}{\Omega}, \quad \phi = \delta^{2/3} \Omega R \tilde{\phi} \quad (11)$$

The use of the tilde is for clarification only, and in the following equations it will not be used.

By defining

$$M = \frac{U}{c_\infty} \quad (12)$$

and introducing a constant Mach number characteristic of the rotational speed of the propeller tip which is defined by

$$M_T = \frac{\Omega R}{c_\infty} \quad (13)$$

the perturbation equation can be derived and is given in scaled coordinates as

$$\begin{aligned} & \left(\frac{M_T \epsilon}{\delta^{1/3}} \right)^2 \frac{\partial^2 \phi}{\partial t^2} + \frac{2MM_T \epsilon}{\delta^{2/3}} \frac{\partial^2 \phi}{\partial y^1 \partial t} + \frac{M^2 - g^{11}}{\delta^{2/3}} \frac{\partial^2 \phi}{(\partial y^1)^2} \\ & + (K+1)MM_T g^{11} \frac{\partial \phi}{\partial y^1} \frac{\partial^2 \phi}{(\partial y^1)^2} = g^{22} \frac{\epsilon^2}{\delta^{2/3}} \frac{\partial^2 \phi}{(\partial y^2)^2} \\ & + g^{33} \frac{\partial^2 \phi}{(\partial y^3)^2} + 2 \left(g^{12} \frac{\epsilon}{\delta^{2/3}} \frac{\partial^2 \phi}{\partial y^1 \partial y^2} \right. \\ & \left. + g^{13} \frac{1}{\delta^{1/3}} \frac{\partial^2 \phi}{\partial y^1 \partial y^3} + g^{23} \frac{\epsilon}{\delta^{1/3}} \frac{\partial^2 \phi}{\partial y^2 \partial y^3} \right) \end{aligned} \quad (14)$$

For low frequency or steady problems, it is admissible to delete the second derivative with respect to time. This gives the final form of the equation in terms of the scaled variables as being

$$\begin{aligned} & \frac{2MM_T \epsilon}{\delta^{2/3}} \frac{\partial^2 \phi}{\partial y^1 \partial t} + \frac{M^2 - g^{11}}{\delta^{2/3}} \frac{\partial^2 \phi}{(\partial y^1)^2} \\ & + (K+1)MM_T g^{11} \frac{\partial \phi}{\partial y^1} \frac{\partial^2 \phi}{(\partial y^1)^2} = g^{22} \frac{\epsilon^2}{\delta^{2/3}} \frac{\partial^2 \phi}{(\partial y^2)^2} \\ & + g^{33} \frac{\partial^2 \phi}{(\partial y^3)^2} + 2 \left(g^{12} \frac{\epsilon}{\delta^{2/3}} \frac{\partial^2 \phi}{\partial y^1 \partial y^2} \right. \\ & \left. + g^{13} \frac{1}{\delta^{1/3}} \frac{\partial^2 \phi}{\partial y^1 \partial y^3} + g^{23} \frac{\epsilon}{\delta^{1/3}} \frac{\partial^2 \phi}{\partial y^2 \partial y^3} \right) \end{aligned} \quad (15)$$

Equation (15) is the small disturbance equation which is solved numerically by the ADI Douglas-Gunn algorithm.

Boundary Conditions

Wall Tangency Condition for Blade Surfaces

The small disturbance boundary condition to be applied at the blade surfaces will now be established. This necessitates returning to the unscaled variables momentarily.

In blade-fixed coordinates, if the equation for the surface of a blade moving in a time-dependent manner is

$$F(y^1, y^2, y^3, t) = 0, \quad (16)$$

then the vanishing of the fluid velocity component normal to the surface brings

$$\frac{D}{Dt} F(y^1, y^2, y^3, t) = \frac{\partial F}{\partial t} + (\bar{a} + \nabla \phi) \cdot \nabla F = 0 \quad (17)$$

where

$$F = F_U(y^1, y^2, y^3, t) = y^3 - h_U(y^1, y^2, t) = 0 \quad (18a)$$

on the upper (suction) blade surface from the leading edge (L.E.) to the trailing edge (T.E.), and

$$F = F_O(y^1, y^2, y^3, t) = y^3 - h_O(y^1, y^2, t) = 0 \quad (18b)$$

on the lower (pressure) blade surface. Here, h is the profile parameter. This follows the convention used for wing surfaces. The coordinates are aligned as shown in Fig. 3, where y^1 is nearly along the mean chord, y^3 is nearly normal to the chord, and y^2 lies in the spanwise direction.

One of the key developments of this work is the generation of coordinate systems possessing the characteristic that $g^{13} \approx 0$ at the blade surfaces. For these coordinate systems, the unsteady boundary condition at the blade surface is simplified.

The general time-dependent boundary condition which allows the profile parameter to include pitching, bending, and twisting is given in scaled variables as

$$\frac{\partial \phi}{\partial y^3} \approx \frac{1}{g^{33}} \left(\epsilon \frac{\partial h}{\partial t} + \frac{M}{M_T} \frac{\partial h}{\partial y^1} \right) \quad (19)$$

This time dependence is included mainly for any future efforts which consider flutter. It is interesting to note that in dimensional Cartesian coordinates ($y^1 = x$, $y^2 = y$, $y^3 = z$), this is the familiar

$$\frac{\partial \phi}{\partial z} \approx \frac{\partial h}{\partial t} + U \frac{\partial h}{\partial x} \quad (20)$$

Finally, the steady scaled boundary condition is simply

$$\frac{\partial \phi}{\partial y^3} \approx \frac{1}{g^{33}} \frac{M}{M_T} \frac{\partial h}{\partial y^1} \quad (21)$$

This boundary condition is not actually applied at the airfoil surfaces but rather at two surfaces separated slightly such that they straddle the mean chord surface which itself lies on, or near, the $y^3 = 0$ surface. Thus, at the upper surface

$$\left. \frac{\partial \phi}{\partial y^3} \right|_{y^3=0+} \approx \frac{1}{g^{33}} \frac{M}{M_T} \frac{\partial h_U}{\partial y^1} \quad (22a)$$

and, at the lower surface

$$\left. \frac{\partial \phi}{\partial y^3} \right|_{y^3=0-} \approx \frac{1}{g^{33}} \frac{M}{M_T} \frac{\partial h_O}{\partial y^1} \quad (22b)$$

Flow Field Boundary Conditions

The upstream boundary condition on the perturbation potential is

$$\phi = 0 \quad (23)$$

This merely states that the free-stream condition prevails sufficiently far upstream.

In the downstream direction, the perturbation potential is not known, but at large distances the condition

$$\frac{\partial \phi}{\partial y^1} = 0 \quad (24)$$

is reasonable and is used as the downstream boundary condition.

At the hub or inner spanwise boundary, the condition

$$\frac{\partial \phi}{\partial y^2} = 0 \quad (25)$$

is used, and the outer spanwise boundary condition is simply

$$\phi = 0 \quad (26)$$

Although y^2 is not strictly a radial direction, it closely approximates it for the coordinate systems employed here.

Above and below the blade, cascade-type periodic boundary conditions are applied such that

$$\phi(y^1, y^2, t) \Big|_{y^3 = \text{upper surface}} = \phi(y^1, y^2, t) \Big|_{y^3 = \text{lower surface}} \quad (27)$$

is satisfied over the boundary surfaces which are chosen to lie at the midchannel between the blades. This, in return for straightforward application, requires a coordinate system which provides nodal coordinates having azimuthal periodicity. Such periodic coordinate systems are discussed in another section.

It remains to discuss the boundary conditions in the vortex wake. Rollup of a wake is ignored and, furthermore, the resulting vortex sheet is approximated as lying between the downstream extensions of the helical surfaces upon which the blade boundary conditions are imposed. The strength of the vortex sheet is assumed to be preserved as it convects downstream. In addition, the direction of the vortex vector is assumed to be "parallel" to the free-stream direction. Since the vortex sheet is a free surface, it cannot support a pressure difference. The boundary condition at the trailing edge can be written in terms of the scaled coordinates as

$$[\phi]_{T.E.} = r(y^2, t) \quad (28)$$

where r is the circulation around the propeller blade, and

$$[\phi] = (\phi)_{y^3=0+} - (\phi)_{y^3=0-} \quad (29)$$

is the jump in the perturbation potential across the wake.

Periodic Helical Coordinate System for Cascades

This section contains the development of special periodic helical coordinates suitable for propeller problems which include cascade effects. The coordinate transformation between this system and an orthogonal Cartesian system is specified so as to provide simple periodic boundaries, and also orthogonal properties at the blades surfaces.

The helical coordinate system used here provides natural surfaces in the form of helicoids which pass through the mean blade locations. This gives convenient surfaces essential to the direct application of blade boundary conditions. Prescribing a second coordinate so as to make it intersect the mean blade surfaces orthogonally, and yet be axially periodic in the circumferential direction, allows both accurate specification of blade boundary conditions and straightforward application of blade periodicity. A third coordinate lies essentially in the radial direction. The helical coordinate system is thereby composed of a coordinate aligned with the mean flow direction, a radial-like coordinate and a coordinate in a circumferential-like direction. Thus, only in the case of the first coordinate direction are the coordinate curves helices. An example of the coordinate system in relationship to a Cartesian one is shown in Fig. 4

The main advantage of these coordinates is that the undisturbed flow direction can be aligned with the helical coordinate direction y^1 . These streamwise helices are constructed such that the helices of greater radii have smaller advance ratios, i.e., the smaller the radius the steeper the spiral, exactly characterizing the mean propeller flow.

To provide circumferential periodicity, the y^3 coordinate must be constructed such that, in a periodic fashion, it repeats its axial locations. The simplest choice is to make y^3 the circumferential direction, forcing it to be independent of the axial value, i.e., identical to the angular coordinate of the familiar circular cylindrical coordinate system. The drawback in doing this is that the y^3 direction would no longer be normal to the streamwise direction. Orthogonality in these two directions is an important quality, especially near the surfaces of the blades. To provide orthogonality at the mean blade locations, the y^3 direction must be perpendicular to the streamwise helices, at least near the blades. Away from the blades, the y^3 coordinate should reverse its axial direction so as to bend back and regain its original axial station. This must be repeated in a periodic fashion about the axis so as to conform to the locations of the blades.

The coordinate direction y^2 which serves to measure the radial value is not, in general, a straight line. This coordinate direction is only a straight line at its coordinate axis, which was chosen to align with the leading edge of one blade, and at the leading edge locations of the remaining blades in the cascade and at lines midway between the leading edges. Only at the leading edge is the coordinate system truly orthogonal. A notable characteristic is that, for high advance ratios, they tend toward orthogonal cylindrical coordinates. This can be easily seen by inspecting the

metric tensors for this transformation which are provided in Appendix A⁷.

A set of helical coordinates which has these properties is given by the following transformation to the Cartesian coordinates x^1 .

$$x^1 = y^2 \sin \theta \quad (30)$$

$$x^2 = y^2 \cos \theta \quad (31)$$

$$x^3 = -\frac{V}{U} y^1 + A(y^2)B(y^3) \quad (32)$$

where θ is the circumferential angle measured as shown in Fig. 4, and which is related to the helical coordinates by

$$\theta = \frac{\Omega}{U} y^1 + \frac{y^3}{y^2} \quad (33)$$

The total helical velocity U is, of course, a function of the radius.

It is convenient to make the following assignments which are consistent with Appendix A of:
 $x^1 = x$, $x^2 = y$, $x^3 = z$ for the Cartesian coordinates and $y^1 = \gamma$, $y^2 = r$, $y^3 = \xi$ for the helical coordinates. Using these replacements the next section will discuss the proper choices for $A(r)$ and $B(\xi)$.

Tailoring the Periodic Helical Coordinates

The functions $A(r)$ and $B(\xi)$ are used to tailor the helical coordinate system to two sets of the streamwise helical sheets. The two sets of sheets of constant ξ are illustrated in Fig. 5. They are evenly spaced in the circumferential direction. The first set of these sheets will contain the mean position of uncambered, symmetric, twisted blades. These correspond to the advance helicoids. The second set of helical surfaces are similar and are chosen such that each sheet lies midway between two neighbors of the first set, thus forming an alternating arrangement of periodically spaced helicoidal surfaces. The boundary conditions for the airfoil surfaces are applied very near members of the first set, whereas the periodic conditions are enforced on the second. It should be mentioned that for asymmetrical blades or blades with camber, the mean blade position will not quite coincide with a helical sheet. The mean blade positions are assumed to lie near the first set of helical sheets so that small disturbance boundary conditions can be accurately applied.

As mentioned, the helical sheets are surfaces of constant ξ . It is desirable for satisfactory application of blade surface boundary conditions that the ξ -coordinate be orthogonal to the mean blade surface. In addition, simple handling of periodicity requires that there be no net change in axial distance when traversing a ξ -coordinate line from one periodic boundary to another. These two objectives can be met by properly choosing the functions $A(r)$ and $B(\xi)$.

Recall that the functions A and B enter the transformation through the relationship given in Eq. (32) which is now written as

$$z = -\gamma \frac{V}{U} + A(r)B(\xi) \quad (34)$$

This specifies the axial coordinate in terms of the helical variables. It will be shown that, by choosing suitable forms for A and B , two of the metric tensors g_{13} and g_{23} become equal to zero concurrently at special values of ξ . The γ and ξ curves will be orthogonal where $g_{13} = 0$ and, likewise, the r and ξ curves will be orthogonal where $g_{23} = 0$. When these are both zero, the ξ curves will be normal to the surfaces of constant ξ . The first objective is to arrange this to occur for those helical sheets containing the mean positions of the propeller blades. To assure that these surfaces are periodically spaced in the circumferential direction, $B(\xi)$ is expressed as the product of two functions of ξ in the form

$$B(\xi) = E(\xi) \frac{\xi_m}{\pi} \sin \left(\frac{\xi}{\xi_m} \pi \right) \quad (35)$$

where E is a damping function and ξ_m is a positive constant establishing the period and is exactly half the distance between the blades.

Meeting the conditions of orthogonality requires the inspection of the functional dependence of g_{13} and g_{23} . This will reveal what the final forms of A and B must be. First, the metric tensor g_{13} will be discussed, and then g_{23} where additional constraints will be imposed on the axial velocity $V(r)$.

From Appendix A,⁷ we have

$$g_{13} = \frac{\Omega r}{U} \frac{r}{R} - \frac{V}{U} A(r)B'(\xi) \quad (36)$$

where the prime indicates differentiation with respect to the indicated argument. By using Eq. (35), this becomes

$$g_{13} = \frac{\Omega r}{U} \frac{r}{R} - \frac{V}{U} A(r) \left[E'(\xi) \frac{\xi_m}{\pi} \sin \left(\frac{\xi}{\xi_m} \pi \right) + E(\xi) \cos \left(\frac{\xi}{\xi_m} \pi \right) \right] \quad (37)$$

As mentioned, E is a damping function and is needed to assure a valid coordinate transformation. A useful form is $E = \exp(-a_0 \bar{\xi}/\xi_m)$. The significance of the over-bar above ξ in the exponential argument will be discussed later.

The derivative E' is

$$E' = \pm \frac{a_0}{\xi_m} \exp \left(-a_0 \left| \frac{\bar{\xi}}{\xi_m} \right| \right) \quad (38)$$

where the minus (plus) sign relates to positive (negative) values of ξ .

By substituting the expressions for E and E' into Eq. (37), we obtain

$$g_{13} = \frac{\Omega r}{U} \frac{r}{R} - \frac{V}{U} A(r) \exp\left(-a_0 \left| \frac{\bar{\epsilon}}{\epsilon_m} \right| \right) \left[\cos\left(\frac{\epsilon}{\epsilon_m} \pi\right) \pm \frac{a_0}{\pi} \sin\left(\frac{\epsilon}{\epsilon_m} \pi\right) \right] \quad (39)$$

with the same meaning as above attached to the sign notation appearing before the last term.

The periodic significance of ϵ_m is now determined by introducing N_B as being a positive integer and allowing the value of ϵ/ϵ_m to range from $-1/2 N_B$ to $1/2 N_B$; here, N_B signifies the number of blades in the cascade and may be either even or odd. Since the value ϵ_m is half the distance between neighboring blades, the blades will be located at intervals of twice ϵ_m . The total distance from $-1/2 N_B$ to $1/2 N_B$ equals one transversal around the cascade. By arbitrarily specifying one blade to be positioned at $\epsilon = 0$, the blade locations take on the following values of ϵ/ϵ_m .

$$\frac{\epsilon_B}{\epsilon_m} = \begin{cases} 0, \pm 2, \pm 4, \dots, \pm(N_B - 1) & ; N_B \text{ odd} \\ 0, \pm 2, \pm 4, \dots, \pm(N_B - 2), N_B & ; N_B \text{ even} \end{cases} \quad (40)$$

where the subscript B denotes a blade location. Also, at this point, the meaning of the over-bar above ϵ is made clear by defining $\bar{\epsilon}$ to be the value of ϵ as measured from the nearest blade. Thus the extremes of $\bar{\epsilon}$ will be $\pm \epsilon_m$. With these definitions Eq. (39) for the metric tensor can be written

$$g_{13} \Big|_{\epsilon=\epsilon_B} = \frac{\Omega r}{U} \frac{r}{R} - \frac{V}{U} A(r) \exp\left(-a_0 \left| \frac{\bar{\epsilon}_B}{\epsilon_m} \right| \right) \left[\cos\left(\frac{\epsilon_B}{\epsilon_m} \pi\right) \pm \frac{a_0}{\pi} \sin\left(\frac{\epsilon_B}{\epsilon_m} \pi\right) \right] \quad (41)$$

for values at the blade stations. However, since $\bar{\epsilon}_B = 0$ from the definition of $\bar{\epsilon}$, and since $\cos(\pi \epsilon_B/\epsilon_m) = 1$ and $\sin(\pi \epsilon_B/\epsilon_m) = 0$, the value of the metric tensor g_{13} for the N_B blade stations reduces to

$$g_{13} \Big|_{\epsilon=\epsilon_B} = \frac{\Omega r}{U} \frac{r}{R} - \frac{V}{U} A(r) \quad (42)$$

Therefore, g_{13} can be forced to equal zero at these periodic positions by simply prescribing that

$$A(r) = \frac{\Omega R}{V} \left(\frac{r}{R}\right)^2 \quad (43)$$

The expression for the axial coordinate can now be explicitly written as

$$z = -\gamma \frac{V}{U} + \frac{\epsilon_m \Omega R}{\pi V} \frac{r^2}{R^2} \exp\left(-a_0 \left| \frac{\bar{\epsilon}}{\epsilon_m} \right| \right) \sin\left(\frac{\epsilon}{\epsilon_m} \pi\right) \quad (44)$$

As mentioned above, the exponential factor serves as a damping function to guarantee that the coordinate transformations are well behaved; i.e., the coordinates should not fold nor should the Jacobian of the transformation vanish anywhere within the region of interest. In this regard, the quantity a_0 is a non-negative constant which increases in magnitude as the ratio $V/\Omega R \equiv$ decreases. For a given λ , the larger the damping the more the ϵ -coordinate is forced to assume a purely circumferential direction.

The expression for the metric tensor g_{23} can be written from Appendix A⁷ as

$$g_{23} = -\frac{\Omega r}{U} \frac{r}{R} \frac{U'(r)}{U} + \left[\left(\frac{V U'(r)}{U^2} - \frac{V'(r)}{U} \right) \gamma + A'(r) B(\epsilon) \right] A(r) B'(\epsilon) \quad (45)$$

From Eq. (35) and the values of ϵ_B , the term $A'(r) B(\epsilon) = 0$ at the N_B blade locations. Furthermore, since g_{13} is zero at these positions, inspection of Eq. (36) indicates that $AB' = (\Omega R/V)(r/R)^2$ at the blades also. Then, for this case, the metric tensor g_{23} reduces to

$$g_{23} \Big|_{\epsilon=\epsilon_B} = -\frac{\Omega r}{U} \frac{r}{R} \frac{U'}{U} + \left(\frac{V U'}{U^2} - \frac{V'}{U} \right) \gamma \frac{\Omega R}{V} \left(\frac{r}{R}\right)^2 = -\frac{\Omega R}{V} \left(\frac{r}{R}\right)^2 \frac{V' \gamma}{U} \quad (46)$$

Requiring V to be a constant is sufficient to render $g_{23} = 0$ since then $V' = 0$. We are in this way able to make g_{23} as well as g_{13} equal to zero at the blade stations defined in Eq. (40).

Thus the ϵ -coordinate lines will be orthogonal to the helical sheets containing the mean camber locations of the blades provided that $A(r)$ and $B(\epsilon)$ are defined as above and that the axial velocity V is a constant. This is no great restriction since a constant value of V is the most reasonable case and the one of most interest.

The second objective is the requirement that the axial distance be the same for corresponding points at each periodic boundary. This is easily verified as being satisfied by inspecting the transformation of z on the helical sheets lying midway between successive blades. From Eq. (44) it is seen that

$$z_{PB} = z \Big|_{\epsilon=\epsilon_{PB}} = -\gamma \frac{V}{U} \quad (47)$$

when

$$\frac{\epsilon}{\epsilon_m} = \frac{\epsilon_{PB}}{\epsilon_m} = \begin{cases} \pm 1, \pm 3, \dots, \pm(N_B - 2), N_B & ; N_B \text{ odd} \\ \pm 1, \pm 3, \dots, \pm(N_B - 1) & ; N_B \text{ even} \end{cases}$$

where the subscript PB denotes "periodic boundary." This relation shows that the net axial distance is not changed upon complete traversal via a ϵ -coordinate line from any periodic sheet to any other. In fact, moving a value of twice ϵ_m along any ϵ -coordinate restores the original axial location. That this is true can be seen by

inspecting Eq. (44). The consequence of this is that any set of sheets separated by a value equal to the blade spacing $2\epsilon_m$ could be used as periodic boundary sheets.

Final Form of the Periodic Helical Coordinates

For convenience, the transformation of the helical coordinates $\gamma = y^1, r = y^2, \epsilon = y^3$ to the Cartesian coordinates $x = x^1, y = x^2, z = x^3$ is given in terms of the nonsuperscripted variables

$$x = r \sin \left(\frac{\Omega}{U} \gamma + \frac{\epsilon}{R} \right) \quad (48)$$

$$y = r \cos \left(\frac{\Omega}{U} \gamma + \frac{\epsilon}{R} \right) \quad (49)$$

$$z = -\gamma \frac{V}{U} + \frac{\epsilon_m}{\pi} \frac{\Omega R}{V} \frac{r^2}{R^2} \exp \left(-a_0 \left| \frac{\epsilon}{\epsilon_m} \right| \right) \sin \left(\frac{\epsilon}{\epsilon_m} \pi \right) \quad (50)$$

This is the set of coordinates which is used in the solution of the small disturbance equation.

Various other cases of these coordinates could have been specified. For example, if either $A(r)$ or $B(\epsilon)$ of Eq. (32) were chosen equal to zero, then the ϵ -curves become circles about the z -axis. As another special case, if $B(\epsilon) = \epsilon$ is chosen, then the ϵ -curves are helices. On each ϵ -helix the coordinate value varies as the arc length divided by the value of the radius at which that given helix lies. This distinguishes them from the streamwise helices which measure as the arc length. The metric tensors are given in the latter part of Appendix A for these special cases.

Numerical Approach

This section presents a general description of the numerical approach used to solve the small disturbance Eq. (38). For the sake of convenience, the small disturbance equation will be rewritten letting $y^1 = \gamma, y^2 = r$, and $y^3 = \epsilon$, as in the last section. With this notation Eq. (38) can be written

$$A_1 \frac{\partial^2 \phi}{\partial \gamma \partial t} = \frac{\partial}{\partial \gamma} \left[A_2 \left(\frac{\partial \phi}{\partial \gamma} \right)^2 + A_3 \frac{\partial \phi}{\partial \gamma} \right] + A_4 \frac{\partial^2 \phi}{\partial r^2} + A_5 \frac{\partial^2 \phi}{\partial \epsilon^2} + A_6 \frac{\partial^2 \phi}{\partial \gamma \partial r} + A_7 \frac{\partial^2 \phi}{\partial \gamma \partial \epsilon} + A_8 \frac{\partial^2 \phi}{\partial r \partial \epsilon} \quad (51)$$

where

$$A_1 = \frac{2MM_T \epsilon}{\delta^{2/3}} \quad (52a)$$

$$A_2 = -\frac{1}{2} (\kappa + 1) MM_T g^{11} \quad (52b)$$

$$A_3 = \frac{g^{11} - M^2}{\delta^{2/3}} \quad (52c)$$

$$A_4 = \frac{2}{\delta^{2/3}} g^{22} = \frac{\epsilon^2}{\delta^{2/3}} \quad (52d)$$

$$A_5 = g^{33} \quad (52e)$$

$$A_6 = \frac{2\epsilon}{\delta^{2/3}} g^{12} \quad (52f)$$

$$A_7 = \frac{2}{\delta^{1/3}} g^{13} \quad (52g)$$

$$A_8 = \frac{\epsilon}{\delta^{1/3}} g^{23} \quad (52h)$$

In transferring the two terms on the left-hand side of Eq. (38) to the right-hand side in Eq. (51), they have been lumped together with the understanding that the variation of g^{11} with respect to γ is small; recall that M is only a function of r and, therefore, the only dependence of A_2 or A_3 on γ is through g^{11} .

It is convenient to define the two bracketed terms above by F so that

$$F_\gamma = \frac{\partial}{\partial \gamma} \left[A_2 \left(\frac{\partial \phi}{\partial \gamma} \right)^2 + A_3 \frac{\partial \phi}{\partial \gamma} \right] \quad (53)$$

Equation (51) is then written as

$$A_1 \frac{\partial^2 \phi}{\partial \gamma \partial t} = F_\gamma + A_4 \frac{\partial^2 \phi}{\partial r^2} + A_5 \frac{\partial^2 \phi}{\partial \epsilon^2} + A_6 \frac{\partial^2 \phi}{\partial \gamma \partial r} + A_7 \frac{\partial^2 \phi}{\partial \gamma \partial \epsilon} + A_8 \frac{\partial^2 \phi}{\partial r \partial \epsilon} \quad (54)$$

Except for the addition of the last two terms above, this equation has the same form as the equation solved in Isom⁵ where an ADI method based on the Douglas-Gunn algorithm was used to solve the finite difference form of the equation for flow about helicopter rotors. The additional cross-derivative terms will be handled by generalizing the Douglas-Gunn algorithm. With modest changes this allowed the numerical code developed for the helicopter problem to be used for the present work.

It should be pointed out that Eq. (54) remains expressed in terms of unstretched physical variables. No mapping of the coordinate system has been carried out so as to produce a nonuniform grid. For simplicity, the numerical algorithm will be presented for the case of no coordinate stretching. Following this, the method of introducing coordinate stretching will be explained.

ADI Douglas-Gunn Algorithm

For three dimensions the ADI technique involves splitting the given equation into three separate finite difference equations which can be solved successively to complete one time-step increment. A current estimate of ϕ , say, ϕ^n is advanced to ϕ^{n+1} through two intermediate values, which will be denoted by ϕ^* and ϕ^{**} , to complete a single stage of iteration.

To begin an iteration at time step n , ϕ^n is advanced to ϕ^* by solving the first equation with only the γ -direction being differenced implicitly; this is called the γ -sweep. Next, in the r -sweep, ϕ^* is advanced to ϕ^{**} by solving

the second equation with only the r -direction being implicit. Finally, in the ξ -sweep, φ^{**} is advanced to φ^{n+1} by solving the third equation with the ξ -direction being the only implicit direction.

The three equations for the respective sweeps are given for a uniform grid as

γ -SWEEP:

$$\frac{A_1}{\Delta t} \delta_\gamma (\varphi^* - \varphi^n) = D_\gamma F_I + A_4 \delta_{rr} \varphi^n + A_5 \delta_{\xi\xi} \varphi^n + A_6 \delta_{\gamma r} \varphi^n + A_7 \delta_{\gamma\xi} \varphi^n + A_8 \delta_{r\xi} \varphi^n \quad (55a)$$

r -SWEEP:

$$\frac{A_1}{\Delta t} \delta_\gamma (\varphi^{**} - \varphi^n) = D_\gamma F_I + \frac{A_4}{2} \delta_{rr} (\varphi^{**} + \varphi^n) + A_5 \delta_{\xi\xi} \varphi^n + \frac{A_6}{2} \delta_{\gamma r} (\varphi^{**} + \varphi^n) + A_7 \delta_{\gamma\xi} \varphi^n + A_8 \delta_{r\xi} \varphi^n \quad (55b)$$

ξ -SWEEP:

$$\frac{A_1}{\Delta t} \delta_\gamma (\varphi^{n+1} - \varphi^n) = D_\gamma F_I + \frac{A_4}{2} \delta_{rr} (\varphi^{**} + \varphi^n) + \frac{A_5}{2} \delta_{\xi\xi} (\varphi^{n+1} + \varphi^n) + \frac{A_6}{2} \delta_{\gamma r} (\varphi^{**} + \varphi^n) + \frac{A_7}{2} \delta_{\gamma\xi} (\varphi^{n+1} + \varphi^n) + \frac{A_8}{2} \delta_{r\xi} (\varphi^{n+1} + \varphi^n) \quad (55c)$$

where D_γ is a special difference operator to be explained below and $\delta_{rr}, \delta_{\xi\xi}, \dots, \delta_{r\xi}$ are standard difference operators in the indicated directions. Here, F represents the bracketed terms of Eq. (51) which correspond to the flux in the γ -direction, and $D_\gamma F_I$ gives the finite difference approximation to $\partial F / \partial \gamma$ at the I^{TH} node for each set of values of J and K . The nodal values I, J and K are associated with the γ, r and ξ directions, respectively. The three directions, have uniform step-sizes $\Delta\gamma, \Delta r$ and $\Delta\xi$, which may be distinct.

An example of how the difference operators in Eq. (55) are defined in terms of difference approximations is

$$\delta_{rr} \varphi^n = \frac{1}{(\Delta r)^2} \left(\varphi_{I,J+1,K}^n - 2\varphi_{I,J,K}^n + \varphi_{I,J-1,K}^n \right) \quad (56)$$

An analogous expression holds for $\delta_{\xi\xi}$. In the case of the mixed second order operators the following is used:

$$\delta_{\gamma r} \varphi^n = \frac{1}{\Delta\gamma \Delta r} \left(\varphi_{I,J+1,K}^n - \varphi_{I,J,K}^n - \varphi_{I-1,J+1,K}^n + \varphi_{I-1,J,K}^n \right) \quad (57)$$

Corresponding expressions hold for $\delta_{\gamma\xi}$ and $\delta_{r\xi}$.

The nonlinear term contained in $D_\gamma F_I$ is linearized by averaging at the n and $*$ time levels by defining

$$F_{I+1/2} = A_2 \left(\delta_\gamma \varphi_{I,J,K}^n \right) \left(\delta_\gamma \varphi_{I,J,K}^* \right) + \frac{1}{2} A_3 \delta_\gamma \left(\varphi_{I,J,K}^n + \varphi_{I,J,K}^* \right) \quad (58)$$

to be the flux at the midpoint of the I^{TH} -cell on any node line given by J and K . The Murman-Cole type-dependent differencing scheme is introduced to provide stable differencing by defining

$$D_\gamma F_I = \frac{1}{\Delta\gamma} \left[\epsilon_I (F_{I+1/2} - F_{I-1/2}) + (1 - \epsilon_{I-1}) \times (F_{I-1/2} - F_{I-3/2}) \right] \quad (59)$$

where

$$\epsilon_I = \begin{cases} 1, & V_c > 0 \\ 0, & V_c < 0 \end{cases} \quad (60)$$

and

$$V_c = A_2 \frac{\partial \varphi}{\partial \gamma} + A_3 \quad (61)$$

This switches the difference equations at each grid point according to whether the flow field at that point is subsonic, sonic, supersonic, or a shock.

A more convenient set of equations for numerical computations is obtained from the set (55) by subtracting Eq. (55a) from Eq. (55b), and Eq. (55b) from Eq. (55c), giving, with some rearrangement, the following set:

γ -SWEEP:

$$\frac{A_1}{\Delta t} \delta_\gamma (\varphi^* - \varphi^n) - D_\gamma F_I = A_4 \delta_{rr} \varphi^n + A_5 \delta_{\xi\xi} \varphi^n + A_6 \delta_{\gamma r} \varphi^n + A_7 \delta_{\gamma\xi} \varphi^n + A_8 \delta_{r\xi} \varphi^n \quad (62a)$$

r -SWEEP:

$$\left(\frac{A_1}{\Delta t} \delta_\gamma - \frac{A_4}{2} \delta_{rr} - \frac{A_6}{2} \delta_{\gamma r} \right) (\varphi^{**} - \varphi^*) = \left(\frac{A_4}{2} \delta_{rr} - \frac{A_6}{2} \delta_{\gamma r} \right) (\varphi^* - \varphi^n) \quad (62b)$$

ξ -SWEEP:

$$\left(\frac{A_1}{\Delta t} \delta_\gamma - \frac{A_5}{2} \delta_{\xi\xi} - \frac{A_7}{2} \delta_{\gamma\xi} - \frac{A_8}{2} \delta_{r\xi} \right) (\varphi^{n+1} - \varphi^{**}) = \left(\frac{A_5}{2} \delta_{\xi\xi} + \frac{A_7}{2} \delta_{\gamma\xi} + \frac{A_8}{2} \delta_{r\xi} \right) (\varphi^{**} - \varphi^n) \quad (62c)$$

The Eq. (62) are in the so-called delta form where the unknowns on the left-hand sides are expressed as differences in the potential. This form has superior numerical properties as compared to Eq. (55). The solution to the above set of equations involve no more than solving tridiagonal matrices, except in the case of a shock point where a quadradiagonal matrix occurs in the γ -sweep.

The potential at time level $n + 1$ can be found from the potential at level n by adding the solutions for the delta differences from all sweeps to ϕ^n as

$$\phi^{n+1} = \phi^n + (\phi^* - \phi^n) + (\phi^{**} - \phi^*) + (\phi^{n+1} - \phi^{**}) \quad (63)$$

As is common in ADI methods, the time step is varied from iteration to iteration over the course of the calculation from some maximum value Δt_{\max} to some minimum value Δt_{\min} . This is done to improve the convergent rate of the calculation. The geometric sequence

$$\Delta t_i = \Delta t_{\min} \left(\frac{\Delta t_{\max}}{\Delta t_{\min}} \right)^{\frac{i-1}{N-1}} \quad i = 1, 2, 3, \dots, N \quad (64)$$

is used for N iterations ($N = 8$) and then repeated until the total number of iterations has been reached. The total number of iterations is determined by a preset value for the maximum number of iterations, or by either satisfying a convergence criteria or exceeding an error bound. The range in the time step for the sequence of iterations addresses both high and low frequency components of the error. In general, the range of Δt_{\min} and Δt_{\max} must be determined by trial and error and is strongly influenced by the size of the computational mesh.

Grid Stretching

Up until now the mesh has been considered to be a uniform grid. However, it is preferable to have the grid points clustered in regions of high gradients and sparsely distributed in regions of low gradients. Grid stretching is a means of accomplishing this. It is used here to distribute the physical coordinates near the airfoil with the greatest concentrations near the leading and trailing edges. The grid is smoothly stretched from the airfoil surfaces to a coarse grid at the outer boundaries of the flow field. The stretching is performed in all three coordinate directions. It is defined in a general sense as a mapping of the physical space $\gamma r \epsilon$ to a uniform computational space $\bar{\gamma} \bar{r} \bar{\epsilon}$ by

$$\gamma = \gamma(\bar{\gamma}, \bar{r}), \quad r = r(\bar{r}), \quad \epsilon = \epsilon(\bar{\epsilon}) \quad (65)$$

It should be noted that the physical coordinates r and ϵ are stretched by their respective computational coordinate. However, γ is a function of both $\bar{\gamma}$ and \bar{r} . the added dependence of γ on \bar{r} is necessary to accommodate swept wings.

The coordinate stretching is introduced through the familiar chain rule formulas. By replacing the various partial derivatives in Eq. (51) with those obtained by the chain rule, this equation is generalized to stretched grids. The use of coordinate stretching complicates, but does not change, the basic form of the ADI algorithm.

Discussion and Results

This discussion focuses on the results obtained for flow surrounding a single blade of an eight

bladed cascade. As explained in the introduction, the blades of this cascade are simple bicircular arc profiles with a maximum blade thickness of five percent. Furthermore, the planform of the blades is rectangular with the required spanwise twist made about the leading edge. This produces a blade of constant chord length. The aspect ratio of the blades is defined as the ratio of the blade-tip radius, as measured from the axis, divided by the chord length. All the results here are for an aspect ratio of 4:1. The hub of the propeller system is placed at a radius of $0.375 R$, where R is the tip radius; this gives an effective aspect ratio of 2.5 for a blade length measured from the hub, rather than from the axis.

The following flows were computed: (1) high advance ratio $\lambda = 100$ with a helical free-stream Mach number at the blade tip of $M_R = 0.8$ and an angle of attack $\alpha = 0.0^\circ$; (2) advance ratio $\lambda = 1$ with $M_R = 0.8$ and $\alpha = 0.0^\circ$; (3) advance ratio $\lambda = 1$ with $M_R = 1.1$ and $\alpha = 0.0^\circ$, and (4) advance ratio $\lambda = 1$ with $M_R = 1.1$ and $\alpha = 2.0^\circ$. The first three cases were compared against results from an Euler code.⁸

Before discussing the results of these cases, the grids used in the computations for the helical small disturbance (HSD) code and the Euler code will be discussed.

Mesh lines for the HSD computations are shown (for the case $\lambda = 1$) in Fig. 6 where, for clarity, only every third line is included from the leading edge to the trailing edge. A uniform grid is used over the blade surface, and a stretched grid is used in the following regions: from the leading edge to the upstream boundary, from the trailing edge to the downstream boundary, from the blade tip to the outer radial boundary, and from the blade surface to the periodic boundary. The grid contained 31 points along the blade in the streamwise direction and an additional 11 grid points both before and after the blade, for a total of 53 streamwise points. In the radial direction, 22 grid points were used with half of these being on the blade. In the circumferential direction, 22 points were used from the lower to the upper periodic boundary. The total grid, therefore, was $53 \times 22 \times 22$.

For the Euler computation, the same unstretched grid was used over the blade surface. Otherwise, the grid was stretched as above but with a different stretching function and, no stretching was used in the circumferential direction. The grid is shown in Fig. 7 for the case of $\lambda = 1$. The position of the blade is indicated by the narrow opening (visible in Fig. 7(b)) of the grid lines near the hub. The grid of Fig. 7(c) illustrates how the streamwise grid transitions from the axial direction upstream of the blade to a helical direction and back again to an axial direction downstream. Since the blade-to-blade direction is purely circumferential, this results in a high degree of coordinate shearing at axial locations near the blade. In addition, the chordwise distribution of grid points is not symmetric front to back along the blade surface, nor is it symmetric from the suction to the pressure side; this asymmetry increases with blade thickness and stagger. The total grid is $59 \times 21 \times 21$ for the case of $\lambda = 100$, and $62 \times 21 \times 21$ for the case of $\lambda = 1$.

The above grids are coarse and the computational solutions given below will be discussed with the understanding that these are preliminary results which should be followed by more detailed calculations.

Case 1) $\lambda = 100$, $M_R = 0.8$, $\alpha = 0^\circ$

This case was chosen to examine what effect blade cascading has on the solution. For the value of $\lambda = 100$, the flow is essentially an axial flow. Since the blade is symmetric from front to back and from top to bottom and $\alpha = 0^\circ$, the solution should reflect this symmetry if no losses occur in the flow field. For the value of $M_R = 0.8$ and the thin 5 percent thick blade, no shocks occurred in the flow field. This expected symmetry is noticeable in the solutions of both the HSD and the Euler codes. Figure 8 shows HSD Mach contours on the blade surface with the minimum contour being 0.75 and the maximum 0.9; the results are identical for the pressure surface and the suction surface. The results reveal the expected drop-off in Mach number with increasing radius. Similar results are shown in Fig. 9 where identical contour values are plotted for the Euler code. The contour shapes obtained from the two codes are very similar with the only essential differences being that the Mach number produced at a given blade location is higher for the HSD code.

Similar symmetry is shown for Mach contours in cross section planes given in Figs. 10 and 11 for the HSD and Euler codes, respectively. Again, the shapes are similar between the two codes, with the HSD results showing more flow acceleration through the passage. The similarity in shapes indicates that qualitatively the HSD solution is being calculated correctly within the interior region of the flow as well as at the blade surfaces.

The solutions on blade-to-blade surfaces are given in Figs. 12 and 13 for the HSD and Euler codes respectively. In each case Mach contours are shown for three different span stations along the blade. The minimum contour value is 0.8. The values of the maximum contours are as follows: 1.0 for Fig. 12(a); 0.92 for Fig. 12(b); 0.86 for Fig. 12(c); 0.88 for Fig. 13(a); and 0.86 for Figs. 13(b) and (c). The results are symmetric and support the above finding that the HSD code predicts flows that agree with the Euler code except in magnitude, at least for subsonic axial flow.

Case 2) $\lambda = 1$, $M_R = 0.8$, $\alpha = 0^\circ$

This case is presented to isolate the effect of blade rotation. The free-stream axial Mach number is only 0.5657, although $M_R = 0.8$. The effect of operating at a low advance ratio is seen in Figs. 14 and 15 which give Mach number contours on the blade surface, again for the HSD and Euler computations, respectively. These contours are given for a range of 0.6 to 0.8 in each case. Other than the expected result that the flow Mach number would increase toward the blade tip, the Euler contours are asymmetric with the pressure surface being nearly the inverted image (left to right) as compared to the suction surface. This might be the result of blade stagger which would give an inverted image for a symmetric blade; for the case of isentropic flow, the Mach number on the pressure surface, at a given chord location,

would be the same as that on the suction surface if its location was measured from the opposite end of the blade. To give an example, the maximum Mach number might occur at 60 percent chord, for a given span station, on the pressure surface; it would then have to occur at 40 percent chord on the suction surface. The reason for the observed difference in the magnitude between the pressure and suction contours for the Euler case is not known but, may in part be due to the grid asymmetry. While the results of the HSD contours are shown to be symmetric, there is no reason that the maximum Mach number must be at midchord.

The blade-to-blade contours for this case are shown in Figs. 16 and 17. The HSD results are given for the following range of Mach contours: 0.6 to 0.66 for Fig. 16(a); 0.66 to 0.71 for Fig. 16(b); and 0.75 to 0.78 for Fig. 16(c). The Euler results are given for the same respective range of Mach contours. The primary difference between the two sets of contours is that the Euler contours more closely resemble contours about isolated blades. In the case of the HSD contours, they tend to shift upstream on the pressure side and downstream on the suction side of the blade so as to gradually join together at midchannel.

Case 3) $\lambda = 1$, $M_R = 1.1$, $\alpha = 0^\circ$

This repeats the previous case except that now the free-stream Mach number is increased so that it has a value of 0.7778 on the axis and a helical free-stream value of 1.1 at the blade tip. The Mach contours on the blade surface are given in Fig. 18 for the HSD computation. The contours are shifted toward the trailing edge on both the pressure and suction surfaces, which show identical contours. Near the tip and trailing edge a very weak shock may exist. In the case of the Euler computations, the rearward shift of peak Mach number is more pronounced. A weak shock probably exists on the suction surface where larger gradients than on the pressure side are indicated.

The blade-to-blade contours for this case are shown in Fig. 20 for the HSD computation and in Fig. 21 for the Euler computation. For both sets of results, the contour levels range from: a) 0.82 to 1.0; b) 0.87 to 1.06 and, c) 0.99 to 1.16. It is not clear that any shock exists for the HSD computation. However, a weak shock is observable in Fig. 21(c) of the Euler computation; it originates near the trailing edge of the suction surface and extends outward to a position upstream of the neighboring blade.

Case 4) $\lambda = 1$, $M_R = 1.1$, $\alpha = 2^\circ$

As a final case, the HSD code was used to recalculate the above case except that a spanwise uniform angle of attack of 2° was used. The Euler code was not used for this case. The Mach contour plots are given in Fig. 22 for the blade surfaces and in Fig. 23 for the blade-to-blade surfaces. The effect of imposing an angle of attack to the blades resulted in a difference between the pressure and suction contours in the expected direction, i.e., the fluid velocity is now higher on the suction side. The blade-to-blade contours reveal that larger regions of the fluid are accelerated on the suction side. Although a weak shock

may exist on either surface, no shock is noted to extend into the fluid from either surface of the blade.

Concluding Remarks and Future Work

The above test cases indicate that although both the HSD and the Euler codes give reasonable solutions, enough differences exist between the two sets of solutions to warrant further investigation. Any future effort should focus on resolving the difference between the two codes in the values of the Mach contours, particularly for case 1. Similarly, the difference between the two for the blade-to-blade contours, with $\lambda = 1$, needs to be explained. As noted above, the mesh used in these calculations was coarse. In addition to the coarseness of the mesh, variations in mesh characteristics exist between the two. Some of the computational differences between the two codes may be resolved if a common mesh is used, and a finer mesh should provide more detailed and accurate computations. As a means of providing a common mesh, a new helical coordinate system is currently being developed which conforms to the blade shape. This means that the small disturbance boundary conditions will be able to be replaced by the actual blade surface boundary conditions. The new coordinate system should also be readily adaptable to the Euler code. This will allow identical grids to be used for both sets of computations. An increased effort will then be invested into exploring areas such as proper specification of the farfield boundary conditions, especially those needed for accurate unsteady calculations.

References

1. Caradonna, F.X. and Philippe, J.J., "The Flow Over a Helicopter Blade Tip in the Transonic Regime," Vertica, Vol. 2, No. 1., 1978, pp. 43-60.

2. Caradonna, F.X. and Isom, M.P., "Subsonic and Transonic Potential Flow Over Helicopter Rotor Blades," AIAA Journal, Vol. 10, No. 12, Dec. 1972, pp. 1606-1612.
3. Caradonna, F.X. and Isom, M.P., "Numerical Calculation of Unsteady Transonic Potential Flow Over Helicopter Rotor Blades," AIAA Journal, Vol. 14, No. 4, Apr. 1976, pp. 482-488.
4. Caradonna, F.X., "The Transonic Flow on a Helicopter Rotor," Ph.D. Thesis, Dept. of Aeronautics and Astronautics, Stanford University, 1978.
5. Isom, M.P. "Unsteady Subsonic and Transonic Potential Flow Over Helicopter Rotor Blades," NASA CR-2463, 1974.
6. Bisplinghoff, R.L., Ashley H., and Halfman R.L., "Aeroelasticity," Addison-Wesley Publishing Co., Cambridge, 1955, Chapter 5.
7. Snyder, A., "Numerical Simulation of Subsonic and Transonic Propeller Flow," Ph.D. Thesis, Dept. of Chemical Engineering, The Univ. of Toledo, June 1987.
8. Celestina, M.L., Mulac, R.A. and Adamcyck, J.J. "A Numerical Simulation of the Inviscid Flow Through a Counterrotating Propeller," Journal of Turbomachinery, Vol. 108, No. 2, Oct. 1986, pp. 187-193.

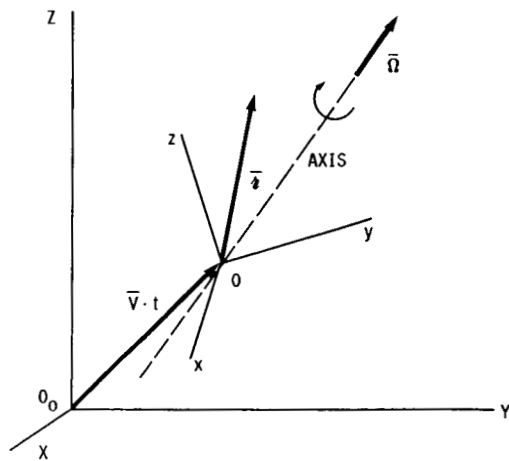


FIGURE 1. - RELATIONSHIP BETWEEN INERTIAL COORDINATE SYSTEM XYZ AND NONINERTIAL COORDINATE SYSTEM xyz WHICH IS ROTATING ABOUT AXIS PASSING THROUGH ITS ORIGIN.

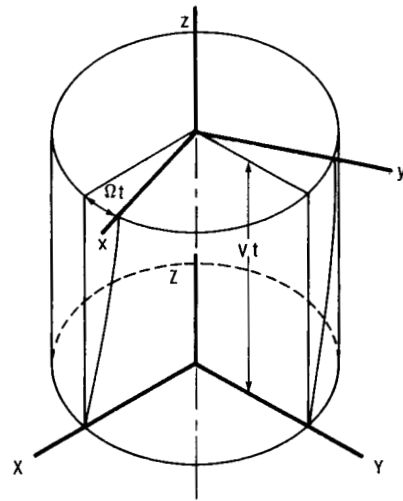


FIGURE 2. - NONINERTIAL COORDINATE SYSTEM xyz ROTATES WITH ANGULAR VELOCITY ABOUT z-AXIS WHICH IS COLINEAR WITH Z-AXIS OF INERTIAL SYSTEM XYZ. THE xyz SYSTEM TRANSLATES WITH AXIAL VELOCITY \$v\$ WITH RESPECT TO THE INERTIAL SYSTEM.

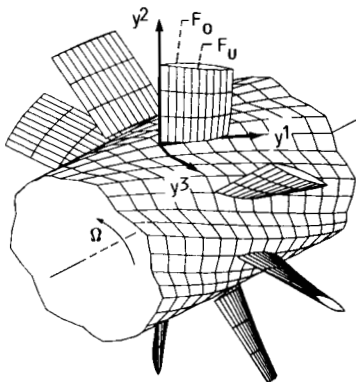


FIGURE 3. - ARRANGEMENT OF HELICAL COORDINATES: THE \$y^1\$-CURVES LIE ALONG THE MEAN FLOW DIRECTION; THE BLADE PROFILE IS GIVEN BY \$F_u\$ ON THE SUCTION SIDE AND BY \$F_o\$ ON THE PRESSURE SIDE; THE FLOW TANGENCY BOUNDARY CONDITION IS NOT APPLIED AT THE BLADE SURFACE BUT RATHER ON TWO COORDINATE SURFACES NEIGHBORING THE MEAN BLADE LOCATION.

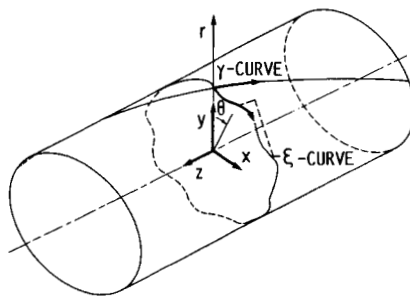


FIGURE 4. - PERIODICAL HELICAL COORDINATES \$\gamma\$ and \$\xi\$ SHOWN WITH CARTESIAN COORDINATES xyz. THE \$\gamma\$-CURVES ARE ESSENTIALLY RADIALLY DIRECTED; THE \$\xi\$-CURVES ARE ESSENTIALLY CIRCUMFERENTIAL BUT BEND SO AS TO BE NORMAL TO THE \$\gamma\$-CURVES AT THE BLADE LOCATIONS. THE ORIGIN OF BOTH SYSTEMS IS ON THE AXIS.

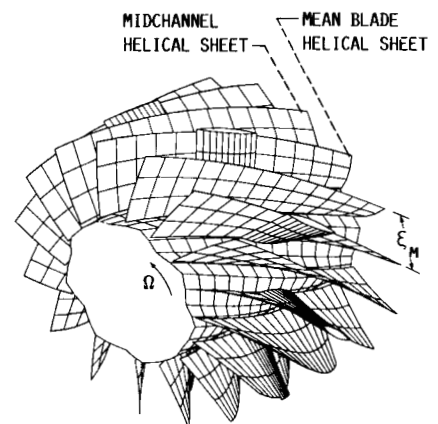


FIGURE 5. - ALTERNATING ARRANGEMENT OF HELICOIDAL SHEETS FOR AN EIGHT BLADED PROPELLER. PERIODIC BOUNDARY CONDITIONS ARE APPLIED AT THE MIDCHANNEL HELICAL SHEETS. THE ANGULAR DISTANCE BETWEEN THE TWO TYPES OF SHEETS IS DENOTED BY \$\epsilon_m\$.

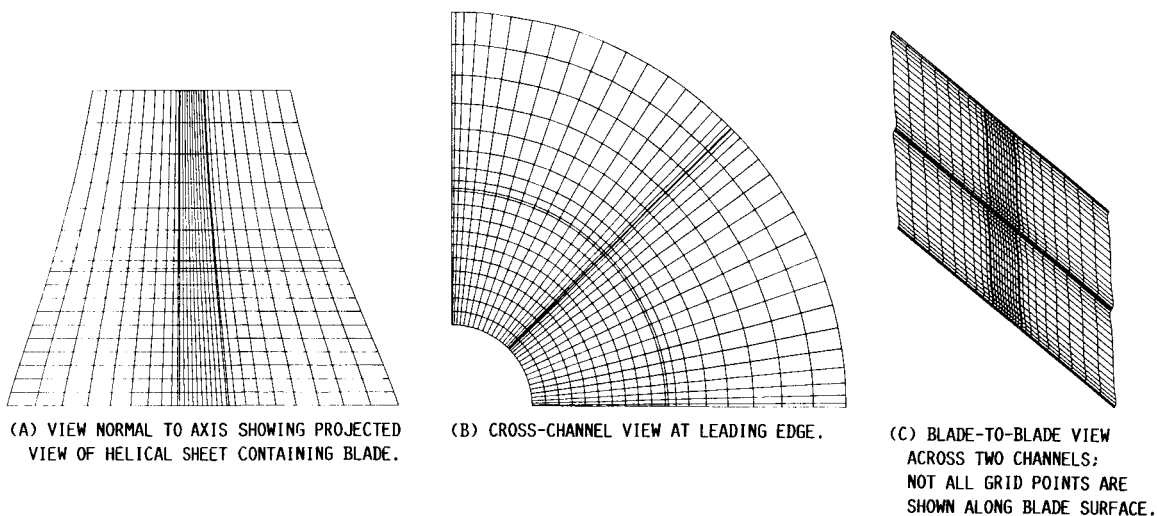


FIGURE 6. - HELICAL COORDINATES USED IN SMALL DISTURBANCE COMPUTATION.

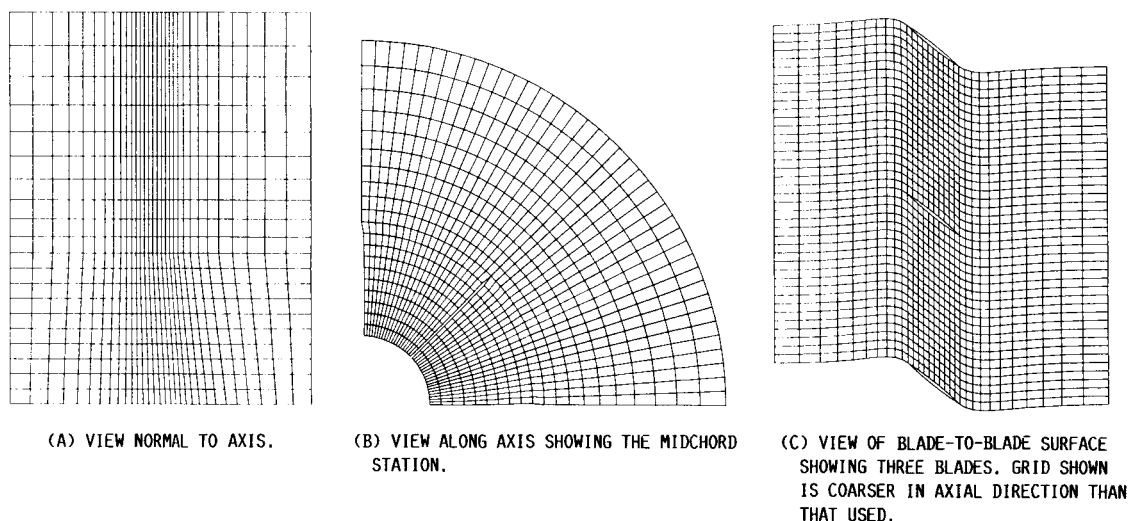


FIGURE 7. - COORDINATES USED IN EULER COMPUTATION.

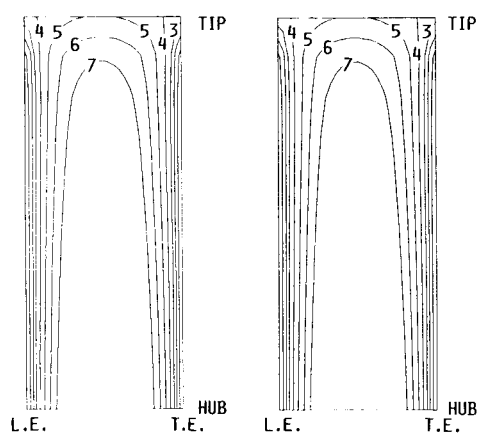


FIGURE 8. - MACH CONTOURS OF SMALL DISTURBANCE COMPUTATION ON BLADE SURFACES; ADVANCE RATIO = RATIO = 100, $M_R = 0.8$, $\alpha = 0^\circ$.

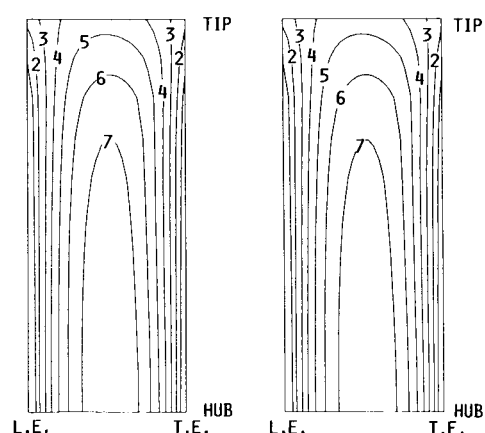


FIGURE 9. - MACH CONTOURS OF EULER COMPUTATION ON BLADES SURFACES; ADVANCE RATIO = 100, $M_R = 0.8$, $\alpha = 0^\circ$.

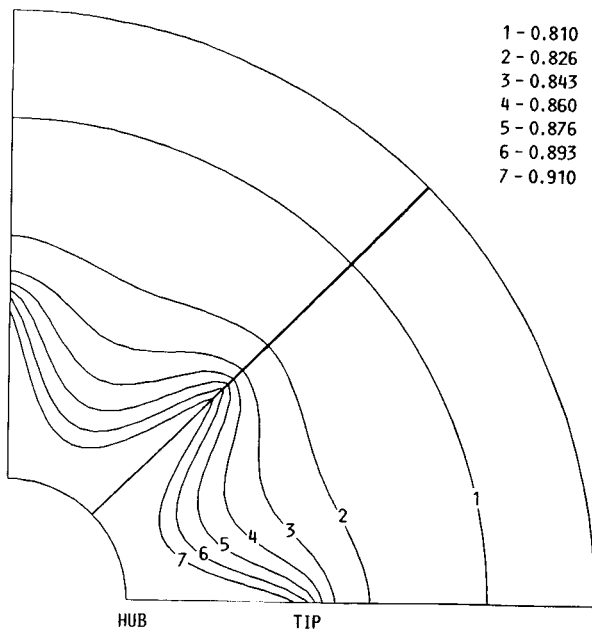


FIGURE 10. - MACH CONTOURS OF SMALL DISTURBANCE COMPUTATION IN CROSS PLANE AT MIDCHORD AXIAL LOCATION: ADVANCE RATIO = 100, $M_R = 0.8$, $\alpha = 0^\circ$.

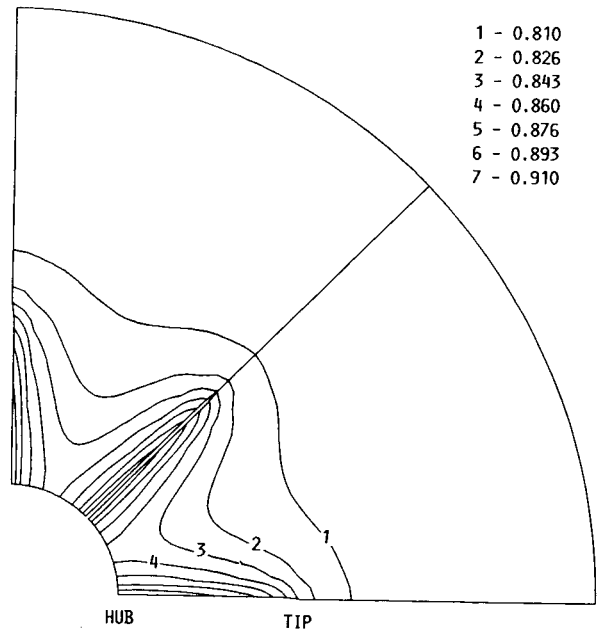


FIGURE 11. - MACH CONTOURS OF EULER COMPUTATION IN CROSS PLANE AT MIDCHORD AXIAL LOCATION: ADVANCE RATIO = 100, $M_R = 0.8$, $\alpha = 0^\circ$.

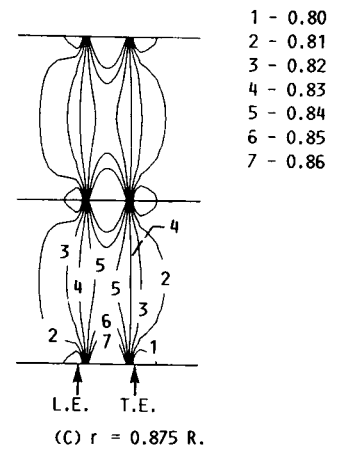
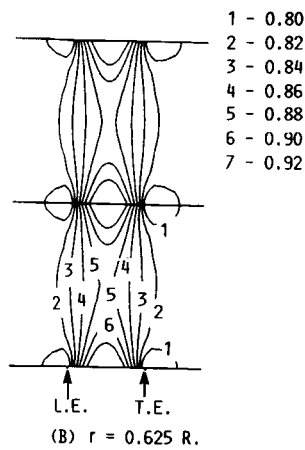
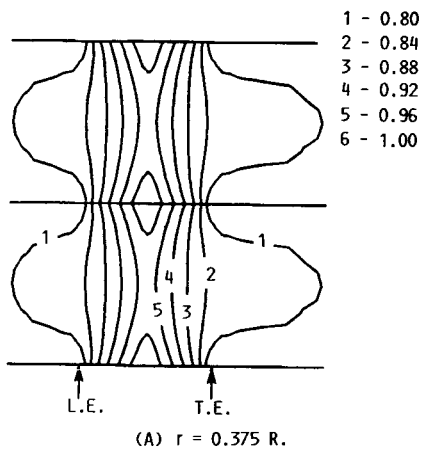


FIGURE 12. - MACH CONTOURS OF SMALL DISTURBANCE COMPUTATION ON BLADE-TO-BLADE SURFACE AT VARIOUS SPAN LOCATIONS: ADVANCE RATIO = 100, $M_R = 0.8$, $\alpha = 0^\circ$.

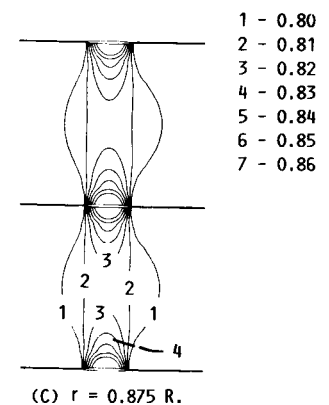
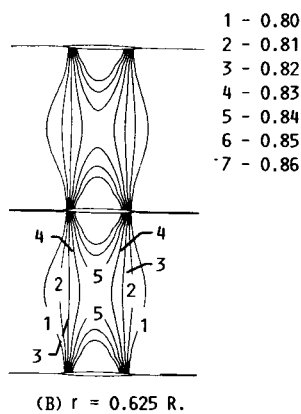
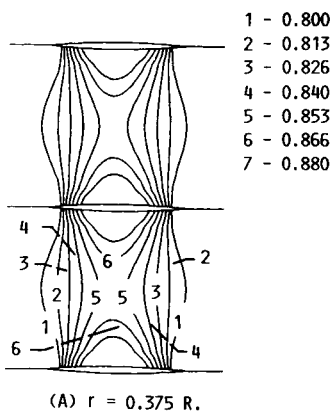


FIGURE 13. - MACH CONTOURS OF EULER COMPUTATION ON BLADE-TO-BLADE SURFACE AT VARIOUS SPAN LOCATIONS: ADVANCE RATIO = 100, $M_R = 0.8$, $\alpha = 0^\circ$.

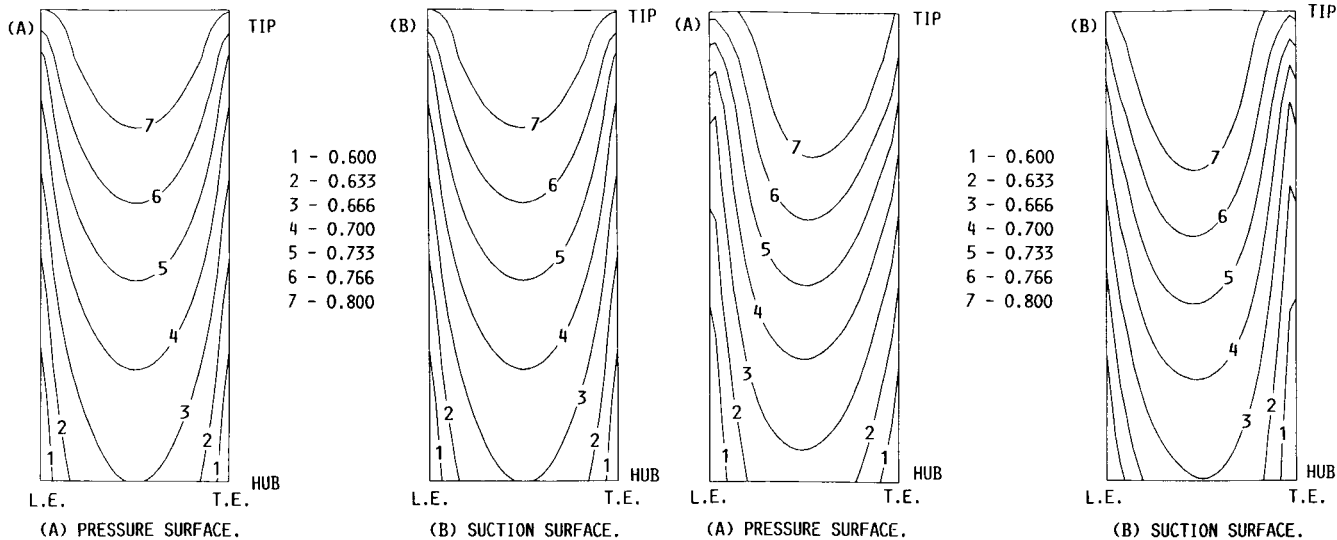


FIGURE 14. - MACH CONTOURS OF SMALL DISTURBANCE COMPUTATION ON BLADE SURFACES: ADVANCE RATIO = 1, $M_R = 0.8$, $\alpha = 0^\circ$.

FIGURE 15. - MACH CONTOURS OF EULER COMPUTATION ON BLADE SURFACES: ADVANCE RATIO = 1, $M_R = 0.8$, $\alpha = 0^\circ$.

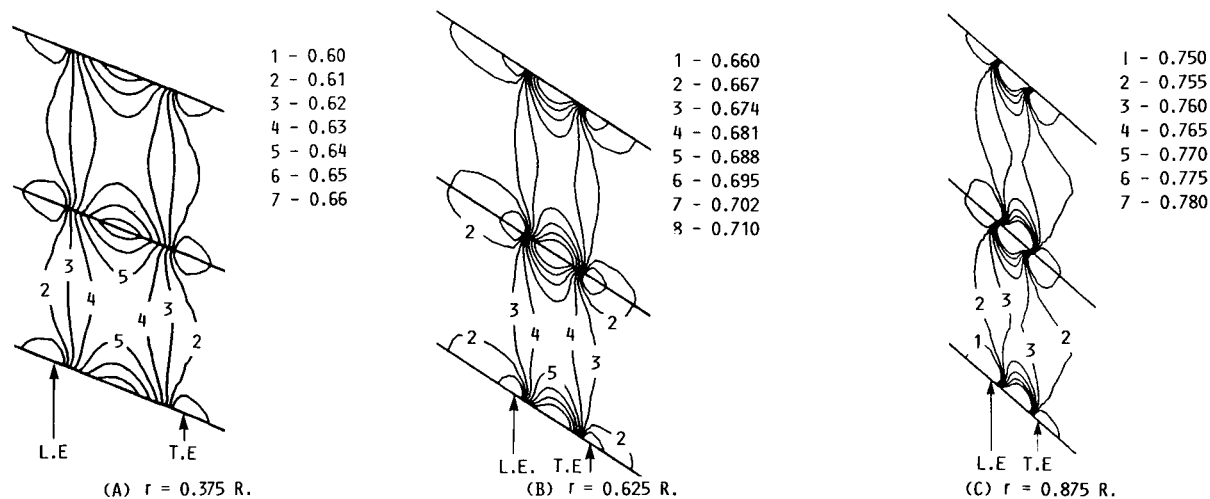


FIGURE 16. - MACH CONTOURS OF SMALL DISTURBANCE COMPUTATION ON BLADE-TO-BLADE SURFACE AT VARIOUS SPAN LOCATIONS; ADVANCE RATIO = 1, $M_R = 0.8$, $\alpha = 0^\circ$.

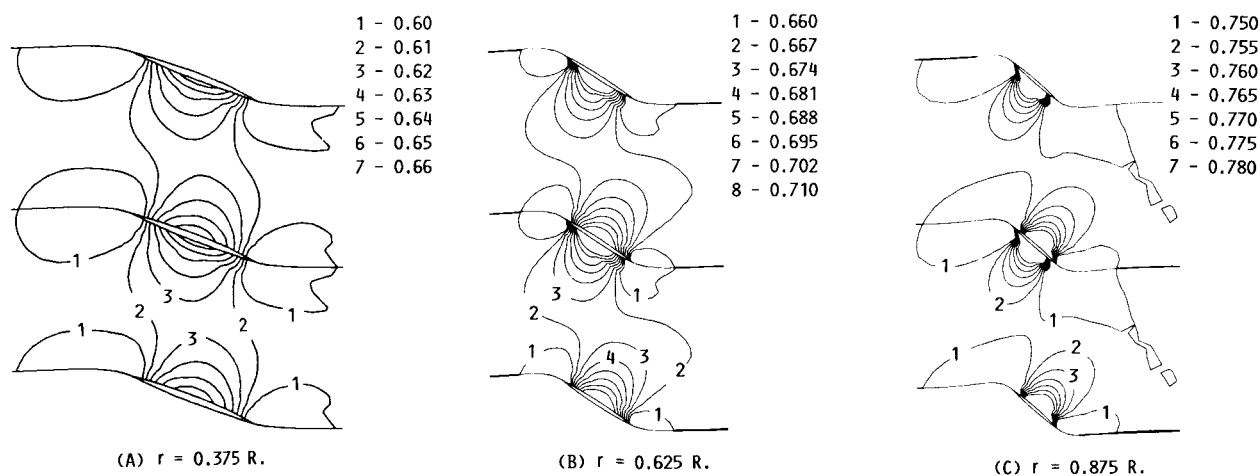


FIGURE 17. - MACH CONTOURS OF EULER COMPUTATION ON BLADE-TO-BLADE SURFACE AT VARIOUS SPAN LOCATIONS; ADVANCE RATIO = 1, $M_R = 0.8$, $\alpha = 0^\circ$.

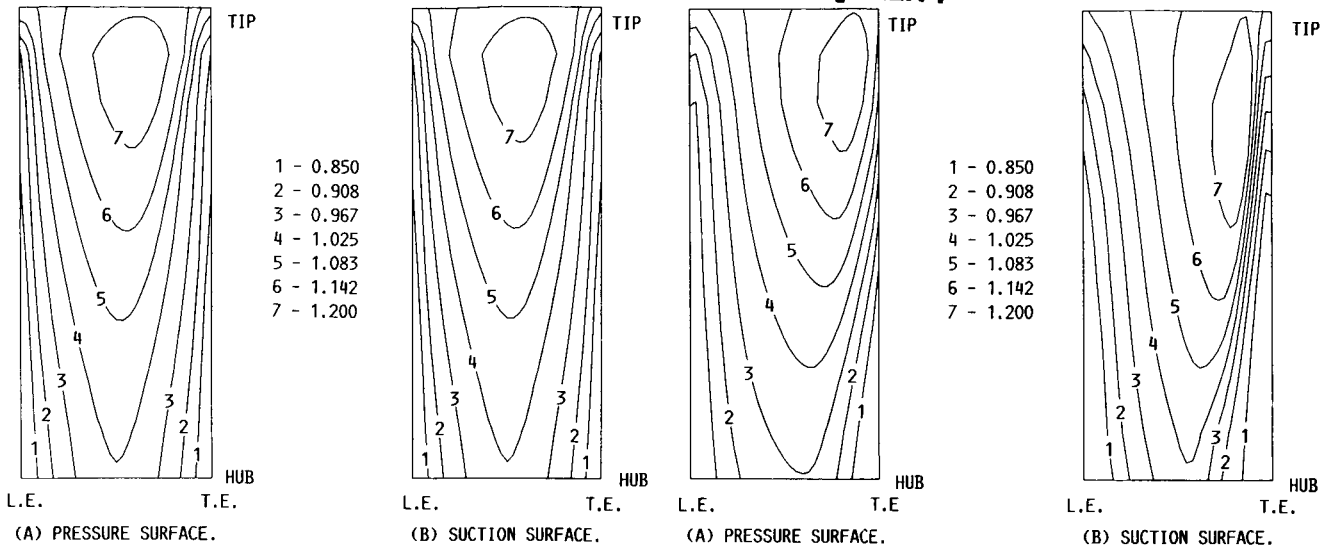


FIGURE 18. - MACH CONTOURS OF SMALL DISTURBANCE COMPUTATION ON BLADE SURFACES; ADVANCE RATIO = 1, $M_R = 1.1$, $\alpha = 0^\circ$.

FIGURE 19. - MACH CONTOURS OF EULER COMPUTATION ON BLADE SURFACES; ADVANCE RATIO = 1, $M_R = 1.1$, $\alpha = 0^\circ$.

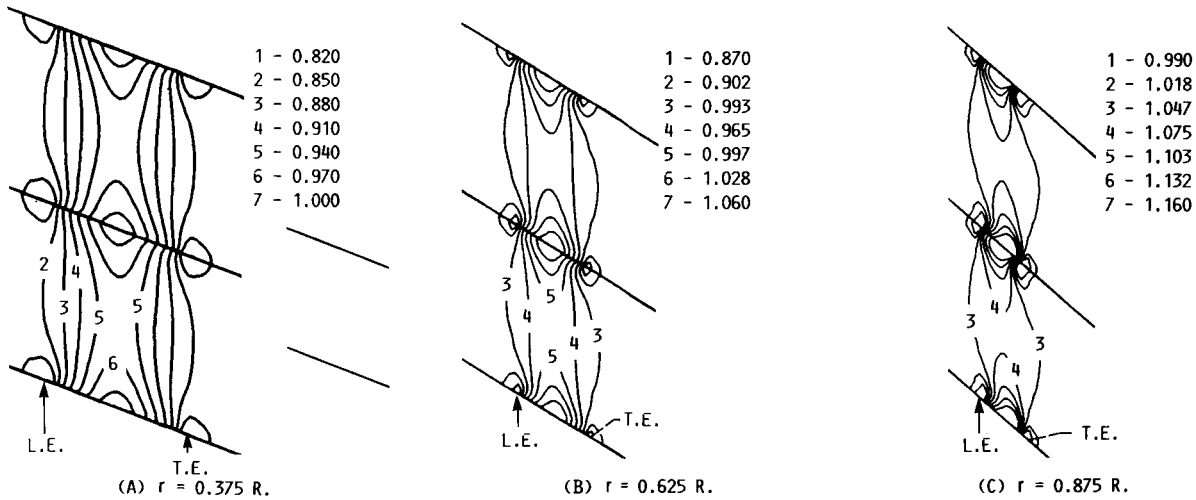


FIGURE 20. - MACH CONTOURS OF SMALL DISTURBANCE COMPUTATION ON BLADE-TO-BLADE SURFACE AT VARIOUS SPAN LOCATIONS; ADVANCE RATIO = 1, $M_R = 1.1$, $\alpha = 0^\circ$.

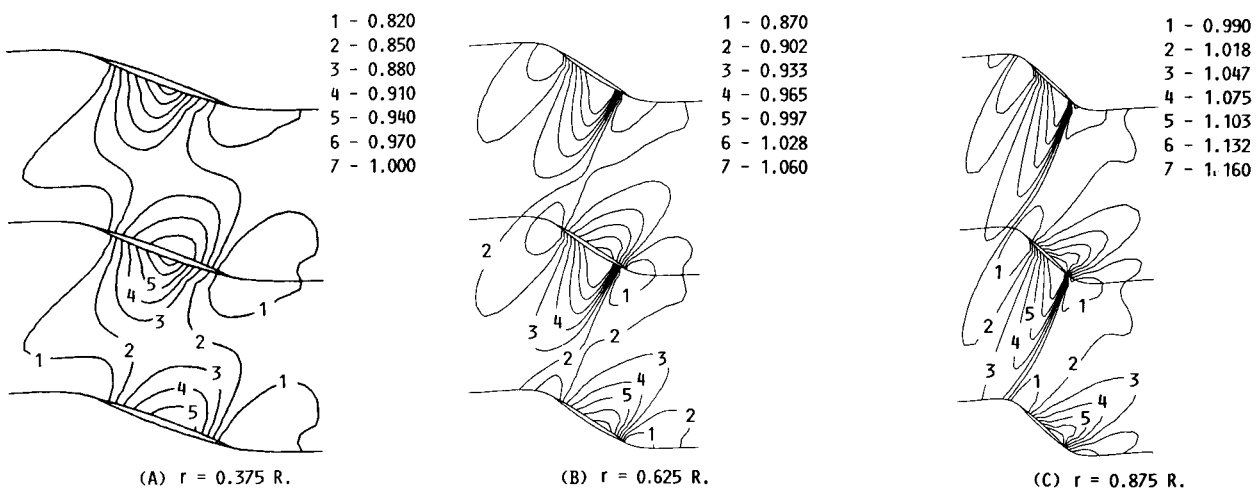


FIGURE 21. - MACH CONTOURS OF EULER COMPUTATION ON BLADE-TO-BLADE SURFACE AT VARIOUS SPAN LOCATIONS; ADVANCE RATIO = 1, $M_R = 1.1$, $\alpha = 0^\circ$.

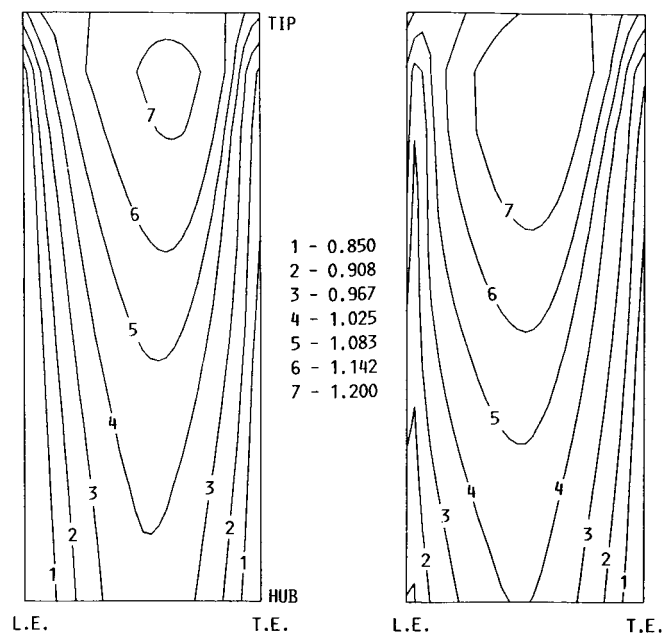


FIGURE 22. - MACH CONTOURS OF SMALL DISTURBANCE ON BLADE SURFACES: ADVANCE RATIO = 1, $M_R = 1.1$, $\alpha = 2^\circ$.

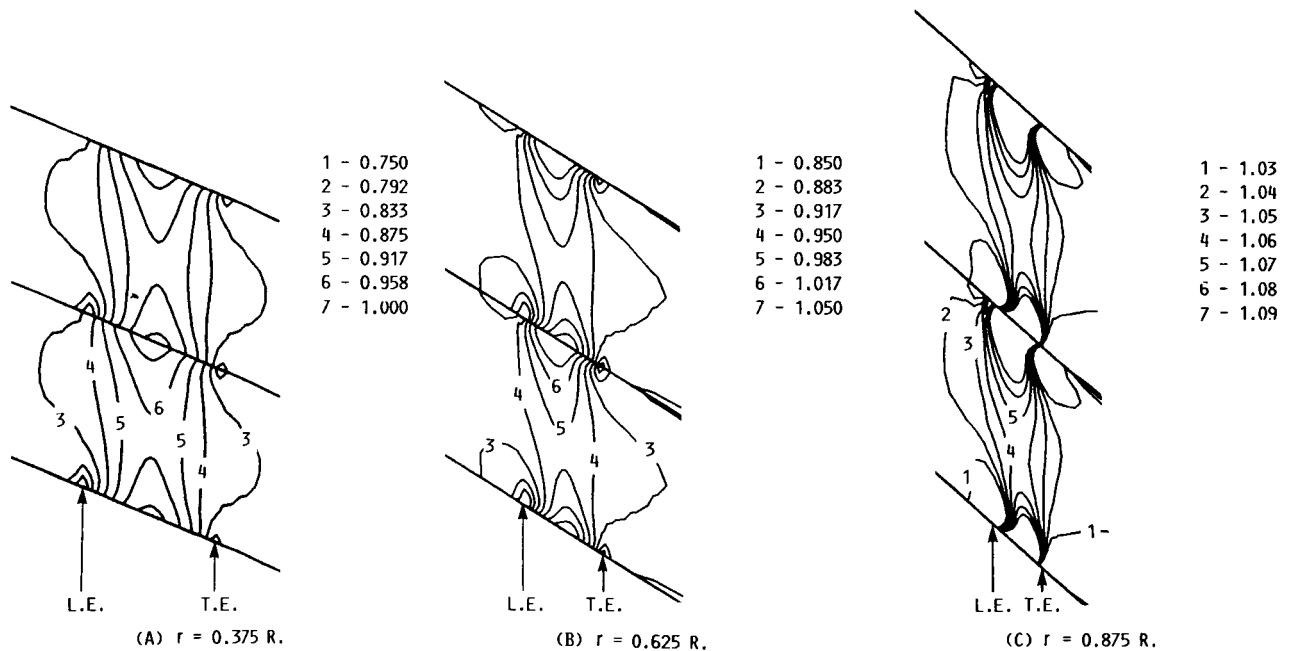


FIGURE 23. - MACH CONTOURS OF SMALL DISTURBANCE COMPUTATION ON BLADE-TO-BLADE SURFACE AT VARIOUS SPAN LOCATIONS: ADVANCE RATIO = 1, $M_R = 1.1$, $\alpha = 2^\circ$.

1. Report No. NASA TM-89826		2. Government Accession No.		3. Recipient's Catalog No.	
4. Title and Subtitle Numerical Simulation of Transonic Propeller Flow Using a Three-Dimensional Small Disturbance Code Employing Novel Helical Coordinates				5. Report Date	
				6. Performing Organization Code 505-62-21	
7. Author(s) Aaron Snyder				8. Performing Organization Report No. E-3475	
				10. Work Unit No.	
9. Performing Organization Name and Address National Aeronautics and Space Administration Lewis Research Center Cleveland, Ohio 44135				11. Contract or Grant No.	
				13. Type of Report and Period Covered Technical Memorandum	
12. Sponsoring Agency Name and Address National Aeronautics and Space Administration Washington, D.C. 20546				14. Sponsoring Agency Code	
15. Supplementary Notes Prepared for the 8th Computational Fluid Dynamics Conference, sponsored by the American Institute of Aeronautics and Astronautics, Honolulu, Hawaii, June 9-11, 1987.					
16. Abstract This paper discusses the numerical simulation of three-dimensional transonic flow about propeller blades. The equations for the unsteady potential flow about propellers is given for an arbitrary coordinate system. From this the small disturbance form of the equation is derived for a new helical coordinate system. The new coordinate system is suited to propeller flow and allows cascade boundary conditions to be straightforwardly applied. A numerical scheme is employed which solves the steady flow as an asymptotic limit of unsteady flow. Solutions are presented for subsonic and transonic flow about a 5 percent thick bicircular arc blade of an eight bladed cascade. Both high and low advance ratio cases are given which include a lifting case as well as nonlifting cases. The nonlifting cases are compared to solutions from a Euler code.					
17. Key Words (Suggested by Author(s)) Numerical simulation Propellers Three-dimensional Small disturbance			18. Distribution Statement Unclassified - unlimited STAR Category 02		
19. Security Classif. (of this report) Unclassified		20. Security Classif. (of this page) Unclassified		21. No. of pages 21	
				22. Price* A02	